Performance of long-chain mid-chain diol based temperature and productivity proxies at test: a five-years sediment trap record from the Mauritanian upwelling

5 Gerard J. M. Versteegh [1,2,3], Karin A. F., Zonneveld[3,4], Jens Hefter[1,3], Oscar E. Romero[3], Gerhard Fischer[4] Gesine Mollenhauer[1,3]

[1]Alfred–Wegener-Institute for Polar and Marine Research, Am Handelshafen 12, D-27570 Bremerhaven, Germany

[2]Department of Physics and Earth Sciences, Jakobs University, Bremen, Bremen, 28759, Germany

[3]MARUM - Zentrum für Marine Umweltwissenschaften, Universität Bremen, Bremen, 28359, Germany

[4]Fachbereich Geowissenschaften, Universität Bremen, Bremen, 28359, Germany

15 *Correspondence to*: Gerard J. M. Versteegh (gerard.versteegh@awi.de)

Abstract. Long-chain mid-chain diol (shortly diol) based proxies obtain increasing interest to reconstruct past upper ocean temperature and productivity. Here we evaluate performance of the sea surface temperature proxies; long chain diol index (LDI), the diol saturation index (DSI) and the diol chain-length index (DCI), productivity/upwelling intensity proxies: the two diol indices DI_R (Rampen et al., 2008) and DI_W (Willmott et al., 2010) and the combined diol index (CDI), as well as the

20 nutrient diol index (NDI) as proxy for phosphate and nitrate levels. This evaluation is based on comparison of the diols in sediment trap samples from the upwelling region off NW Africa collected at 1.28 km water depth with daily satellite derived sea surface temperatures (SST_{SAT}), subsurface temperatures, productivity, the plankton composition from the trap location, monthly PO_4^{3-} and NO_3^- concentrations, wind speed and wind direction from the nearby Nouadhibou airport. The diol based SST reconstructions are also compared the long chain alkenones based $U^{K'}_{37}$ proxy reconstructions (SST_{UK}).

25 At the trap site, most diol proxies lag wind speed (phase φ = 30 days) and can be related to upwelling. Correlation with the abundance of upwelling species and wind speed is best for the DCI, DSI and NDI whereas the DI and CDI perform comparatively poorly.

The nutrient proxy NDI shows no significant correlation to monthly PO_4^{3-} and NO_3^- concentrations in the upper waters and a negative correlation with wind-induced upwelling (r^2=0.28, φ = 32 days) as well as the abundance of upwelling species

30 (r^2=0.38; Table 4). It is suggested that this proxy reflects upwelling intensity rather than upper ocean nutrient concentrations. At the trap site, SST_{SAT} lags wind speed forced upwelling by about 4 months (φ = 129 d). The LDI based SST (SST_{LDI}) correlate poorly ($r^2 = 0.17$) to SST_{SAT} which we attribute to variability in 1,13 diol abundance unrelated to SST such as

productivity. The SST_{UK} correlates best with SST_{SAT} ($r^2 = 0.60$). Also amplitude and absolute values agree very well and the flux corrected SST_{UK} time series average equals the SST_{SAT} annual average.

1 Introduction (as Heading 1)

Upper ocean temperature and productivity reconstructions are important for assessing past climate and environment. For organisms, optimal functioning of their membranes and transport in the cell is crucial and since temperature has a large influence on the solubility and viscosity of lipids, organisms adapt their lipid composition to temperature. Common responses to a decrease in temperature are (1) reducing average chain-length of the lipid molecules, (2) increasing the number of double bonds or (3) the degree of cyclisation (e.g. Suutari et al., 1994; Elling et al., 2015; Sollich et al., 2017). This response of organisms to adapt their metabolism and metabolite composition to prevailing ocean conditions we can use to reconstruct past ocean temperature and productivity through searching for relevant metabolites in the fossil record and taking them as environmental proxies. This is not an unequivocal enterprise since the metabolite composition of organisms is often influenced by a combination of environmental variables and, therefore, proxies based on these metabolites bear the risk of reflecting this. Furthermore, the same metabolites may be produced by different organisms, each having its own complex response to environment. To obtain robust and reliable temperature, nutrient and productivity reconstructions from fossil metabolites it is essential to test the performance of these proxies in present day conditions. In this study, we do so by investigating the long-chain mid-chain diol composition in sediment trap samples in relation to environment during a multiyear trap deployment. We performed this study in the upwelling area off Cape Blanc, one of the most productive regions in the world (Chavez and Messié, 2009). From this region detailed (daily to monthly) records of water temperature, productivity, nutrient concentrations and upwelling dynamics in the upper ocean as well as atmospheric parameters like wind direction and wind intensity are available.

Our study focuses on several diol-based proxies that have been proposed for temperature, productivity and/or upper ocean nutrient concentrations. For temperature these are (1) the Long-chain Diol Index (LDI) (Rampen et al., 2012), (2) the Diol Saturation Index (DSI) (Rampen et al., 2014a) and (3) the Diol Chain length Index (DCI) (Rampen et al., 2009, 2014a). The Combined Diol Index (CDI) (Rampen et al., 2014a) and two Diol Indices (DI), the DI_R (Rampen et al., 2008) and DI_W (Willmott et al., 2010) have been suggested as proxies for upper ocean upwelling/productivity. The Nutrient Diol Index (NDI) has been proposed for reconstructing sea surface nitrate/phosphate concentrations (Gal et al., 2018).

Other diol-based proxies have been defined but these either strongly correlate with the proxies mentioned above or are not relevant in the Mauritanian setting such as a diol proxy for terrestrial/fresh water input (Versteegh et al., 1997; Lattaud et al., 2017a,b). We also evaluate the diol temperature proxies in relation to the lipid based temperature proxies: the long-chain alkenone-based $U^{K'}_{37}$ (Prahl and Wakeham 1987; Brassell et al., 1986a).

1.1 Regional oceanography (as Heading 2)

The Mauritania upwelling system is part of the Canary Current (CC) Eastern Boundary Upwelling Ecosystem (CC–EBUE).

65 The coastal upwelling off Mauretania is driven by the NNW to NNE trade winds and occurs where the southward CC flowing along the coast meets the northward Cap Verde Current (CVC) and Poleward Undercurrent (PUC). These currents are deflected offshore, resulting in the SW directed Cape Verde Frontal Zone (CVFZ) (Fig. 1). The result of this deflection and the offshore water export is visible as the giant Mauritanian chlorophyll filament (Fig. 1 after Romero et al. 2020). As a result of the coastal, shelf and slope topography and the ocean currents and trade winds from the North, the coastal region off

70 Mauritania is characterized by almost permanent upwelling. Its intensity varies throughout the year with maximal intensity and extension in boreal winter and spring (Lathuilière et al., 2008; Cropper et al., 2014; Romero et al., 2020). The offshore transport by the upwelling filaments is considerable and it has been estimated that during periods of intense upwelling 80% of the shelf particular matter production is transported into the open ocean up to 400 km offshore whereas remineralisation and turbulence sustain production and enhanced transport of organic carbon to 2000 km westwards (e.g. Gabric et al., 1993;

75 Lovecchio et al., 2017, 2018).

2 Material and Methods (as Heading 1)

2.1 Sample collection (as Heading 2)

Particulate organic matter forming the base of this study was collected between June 2003 and March 2008 off Cape Blanc at the eutrophic mooring station CBeu (Fig. 1; Table 1). For the trap type and sampling performance see Romero et al. (2020).

80 Classical cone-shaped traps with a surface opening area of 0.5 m^2 were used (Kiel SMT 230/234, Kremling et al., 1998). Over the five years studied, 120 samples were collected in total. Prior to each deployment, sampling cups were poisoned with 1mL of concentrated HgCl2 per 100mL of filtered seawater. Pure NaCl was used to increase the density in the sampling cups up to 40 ‰. Upon recovery, samples were stored at 4 °C and wet split in the MARUM sediment trap laboratory at Bremen University, Bremen, using a rotating McLane wet splitter system. Larger swimmers, such as crustaceans, were

85 handpicked with forceps and removed by carefully filtering through a 1 mm sieve. All flux data hereafter refer to the size fraction of < 1 mm.

2.2 Lipid extraction (as Heading 2)

Lipids were extracted using ultrasonic disruptor probes with successively less polar solvents: MeOH, MeOH–DCM (1:1, v–v) and DCM (after Müller et al., 1998). The TLEs were dried over anhydrous Na$_2$SO$_4$ and saponified with 0.1 M KOH in

90 90/10 MeOH:H$_2$O for 2 hours at 80°C. For desalting, each sample was washed with distilled water and a solution of DCM:MeOH (1:1, vol:vol). The supernatant was removed, the DCM:MeOH phases were rotary evaporated and later dried over anhydrous Na$_2$SO$_4$. Total lipid extracts were saponified with 6% KOH in MeOH at 85°C for 2 h. The neutral lipid

fraction was extracted with hexane, and then fractionated into three polarity fractions using Bond–Elut silica gel cartridges. Fractions 1–3 were eluted in 2mL each of hexane, hexane:dichloromethane 1:2 v–v, and methanol, respectively. For the

95 samples from CBeu 5 androstanol was used as internal standard.

2.3 Lipid data aquisition (as Heading 2)

For diol analyses the polar fractions were silylated with 100 µl N,O–bis (trimethylsilyl) trifluoroacetamide (BSTFA) for 1 hour at 70°C. Except CBeu5 (see below), the concentrations of the different diol isomers were determined using a time of flight mass spectrometer (TOF–MS) LECO Pegasus III (LECO Corp., St. Joseph, MI) interfaced to an Agilent 6890 gas

100 chromatograph (GC). The GC was equipped with a 15m x 0.18mm i.d. Rtx–1MS (Restek Corp., USA) column (film thickness: 0.10µm) with an integrated 5m guard column. A temperature-programmable cooled injection system (CIS4, Gerstel) in combination with an automated liner exchange facility (ALEX, Gerstel) and a multi-purpose autosampler (MPS 2, Gerstel) were used for sample injection. The CIS was operated in solvent vent mode (2.5 µL injection volume) and initially held at 40 °C for 0.05 min, then heated at 12 °C s^{-1} to 80 °C (held 0.1 min) with the split valve open, a vent flow of

105 100 mL min^{-1} and a vent time of 10 sec. After the solvent vent time, the split valve was closed, the CIS heated at 12 °C s^{-1} to 340 °C and held for 2 min for sample transfer to the GC-column. The GC oven was initially held at 60 °C for 1 min, then heated at 50 °C min^{-1} to 250 °C and at 30 °C min^{-1} to 310 °C (held 2.5 min), resulting in an analysis time of 9.3 min per sample. Helium was used as carrier gas in constant flow mode at a rate of 1.5 mL min^{-1}.

The ion source was operated at a temperature of 220 °C with the GC connected to the source by means of a heated transfer

110 line set to 280 °C. The pressure in the flight tube of the MS was 2 x 10^{-7} Torr. Full range mass spectra from m/z 50–600 obtained under EI conditions at 70 eV were recorded at a data rate of 40 spectra s^{-1}. Processing of the TOF–MS data was accomplished with the software (ChromaTOF™) provided by the manufacturer and included automated baseline and peak finding, spectral deconvolution of overlapping chromatographic peaks, peak area calculations, and extraction of compound specific m/z (mass-to-charge ratio) ion chromatograms.

115 Relative amounts of alkyl diol isomers were estimated from peak areas of specific ions resulting from α–cleavage of trimethylsilyl-ethers at various mid-chain positions (de Leeuw et al., 1981) As an example, for C$_{28}$ diols peaks at m/z 299 (1,14-diol) and m/z 313 (1,13-diol), and for C$_{30}$ diols peaks at m/z 313 (1,15 diol) and m/z 327 (1,14-diols) were integrated (Rampen et al., 2008; Versteegh et al., 1997). For the diol quantification, selected reference samples containing alkyl diols in high relative amounts and without other interfering compounds (as indicated by GC/TOF–MS analyses) were analyzed by

120 GC–FID on an Agilent 6890 GC equipped with a 60m x 0.32mm i.d. DB1–MS (Agilent J&W) column (film thickness: 0.25µm). Samples were injected via an on-column injector. The GC oven was initially held at 60 °C for 3 min, and then heated at 20 °C min^{-1} to 150 °C and at 6 °C min^{-1} to 320 °C (held 30 min). Helium was used as carrier gas in constant flow mode at a rate of 1 mL min^{-1}. Alkyl diols were identified by retention times, elution order and relative abundances in comparison to the corresponding GC/TOF–MS analysis. GC–FID areas of the respective diols were used for quantification

125 by comparison to the peak area of an external n-C$_{28}$ 1-alkanol standard. If the diol peaks consisted of a coeluting isomeric

mixture, isomer proportions were quantified by their relative ratios as obtained by analysis of isomer-specific *m/z* ions from GC/TOF–MS. Quantified amounts of diols were than used to obtain mass-specific response factors, that allowed subsequent direct quantification of diols by GC/TOF–MS for the rest of the samples.

The diols of CBeu 5 were analyzed by GC–MS using an Agilent 6850 GC coupled to an Agilent 5975C MSD equipped with
130 a fused silica capillary column (Restek Rxi-1ms; length 30 m; diameter 250 µm; film thickness 0.25 µm). The temperature program for the oven was as follows: held at 60 °C for 3 min, increased to 150 °C at 20 °C min^{-1}, increased to 320 °C at 4 °C min^{-1}, held at 320 °C for 15 min. Helium was used as carrier gas and the flow was held constant at 1.2mL min^{-1}. The MS source was held at 230 °C and the quadrupole at 150 °C. The electron impact ionization energy of the source was 70 eV. Relative amounts of alkyl diol isomers were estimated from peak areas of specific ions as described above. Absolute
135 amounts of diols were obtained by comparison to the peak area of the known amount of the internal standard androstanol (*m/z* 333).

2.4 Calculation of diol indices

Diol indices were calculated on the basis of relative abundances of the diol isomers.

2.4.1 Temperature proxies (as Heading 3)

140 Long Chain Diol Index (Rampen et al., 2012).
$$LDI = 1,15C_{30} / (1,13C_{28} + 1,13C_{30} + 1,15C_{30}) \tag{1}$$
Sea surface temperatures have been calculated based on the following transfer functions:
$$SST = (LDI — 0.095) / 0.033 = 30.3\ LDI — 2.88 \text{ (Rampen et al., 2012)} \tag{2}$$
$$SST = (LDI — 0.1082) / 0.0325 = 30.8\ LDI — 3.33 \text{ (DeBar et al., 2020)} \tag{3}$$
145

Diol Saturation Index (Rampen et al., 2014a)
$$DSI = (1,14C_{28} + 1,14C_{30}) / (1,14C_{28} + 1,14C_{28:1} + 1,14C_{30} + 1,14C_{30:1}). \tag{4}$$
According to Rampen et al. (2014a) this index has a high correlation to temperature in *Proboscia* cultures (Rampen et al., 2009) following the relation:
150 $$T_{culture} = 40\ DSI + 1.2 \tag{5}$$

Diol Chain length Index (Rampen et al., 2009, 2014a)
$$DCI = 1,14C_{30} / (1,14C_{28} + 1,14C_{30}) \tag{6}$$
transfer functions have been published for this index on the basis of *Proboscia* diatom cultures:
155 $$T_{culture} = 50*DCI + 3.95 \tag{7}$$
on the basis of SE Atlantic core top values in relation to summer SST (Rampen et al., 2009):
$$SST_{January}=19.6*DCI + 14.0\ (r^2=0.62, p=3.2\ 10^{-6}) \tag{8}$$

and calculated on the basis of the SE Atlantic data of versteegh et al. (2000):

$$SST_{December} = 22.8*DCI + 6.34 \quad (r^2=0.68, p=1.5\ 10^{-4}) \tag{9}$$

160

The DSI and DCI showed high correlations to culture temperature but these correlations were absent in a global survey relating DSI and DCI derived from core-tops to SST (Rampen et al., 2014a).

2.4.2 Upwelling / upper ocean productivity proxies

Diol Index (Rampen et al., 2008)

165 $$DI_R = (1,14C_{28} + 1,14C_{30}) / (1,14C_{28} + 1,14C_{30} + 1,15C_{30}) \tag{10}$$

This has been suggested as a proxy for southwest monsoon upwelling in the Arabian Sea (Rampen et al., 2008) and is also applicable to the Namibian upwelling (see Versteegh et al., 2000)

Diol Index (Willmott et al., 2010)

170 $$DI_W = (1,14C_{28} + 1,14C_{30}) / (1,14C_{28} + 1,14C_{30} + 1,13C_{28} + 1,13C_{30}) \tag{11}$$

This ratio was designed as a measure of the contribution of *Proboscia* diols relative to other diols.

Combined Diol Index (Rampen et al., 2014a)

$$CDI = (1,14C_{28} + 1,14C_{30}) / (1,13C_{28} + 1,13C_{30} + 1,14C_{28} + 1,14C_{30} + 1,15C_{30}) \tag{12}$$

175 ### 2.4.3 Upper ocean nitrate and phosphate concentration proxies

Nutrient Diol Index (NDI) (Gal et al., 2018)

$$NDI = (1,14C_{28} + 1,14C_{28:1}) / (1,14C_{28} + 1,14C_{28:1} + 1,14C_{30} + 1,14C_{30:1} + 1,13C_{28} + 1,13C_{30} + 1,15C_{30}) \tag{13}$$

$$[PO_4^{3-}] = (NDI - 0.015) / 0.413 = 2.42\ NDI - 0.0363 \tag{14}$$

$$[NO_3^-] = (NDI - 0.075) / 0.026 = 38.5\ NDI - 2.88 \tag{15}$$

180 As may be expected, the ratio of the slopes of these transfer functions is 1:16, the Redfield Ratio (Redfield 1963).

Generally, fluxes recorded in sediment traps have a logarithmic nature. As a result, linear correlations between diols are subject to bias by single high values. To overcome this bias, we based our correlations on the log-transformed diol concentrations (Sup. Fig. S1). Diol concentrations of CBeu1–4 are on average more than one order of magnitude (20.71

185 times) lower than for CBeu5 (Sup. Fig. S2). Although this does not affect the diol proxy ratio's, it does affect the direct comparison of diol fluxes. Concentrations of CBeu1–4 have been calculated without standard but by using the peak areas, response factors, injection volume and sediment mass. In contrast, diol concentrations of CBeu5 have been calculated using peak areas, response factors and an internal standard and these fluxes are in good agreement with those reported from other sediment traps from high productivity regions (Rampen et al., 2008, DeBar et al., 2019). For comparison of diol

190 concentrations between both trap series we multiplied the CBeu1–4 values by 20.71 to agree with those of the better validated CBeu5 concentrations. Obviously, these new values do not represent exact concentrations but they reduce the concentration error considerably whereas the concentration dynamics between the individual samples remain intact (Sup. Fig. S2).

2.5 Alkenone based $U^{K'}_{37}$ SST proxy

195 Lipid SST proxy data on long chain alkenone based $U^{K'}_{37}$ have been determined for trap CBeu5 (material collected between 28 March 2007 and 17 March 2008). Data have been combined with those of Mollenhauer et al. (2015) for CBeu1–4.

The alkenones in fraction 2 were analysed using an Agilent 5890 gas chromatograph equipped with a DB5–MS capillary column and a flame ionization detector. Alkenone identification is by relative retention times and comparison with a laboratory-internal standard sediment. The $U^{K'}_{37}$ index was calculated using the peak areas of the $C_{37:2}$ and $C_{37:3}$ alkenones

200 (Prahl and Wakeham, 1987):

$$U^{K'}_{37} = [C_{37:2}] / ([C_{37:2}] + [C_{37:3}]) \tag{16}$$

Analytical precision based on repeated analyses of the standard sediment is ± 0.01 units of the $U^{K'}_{37}$ index. The $U^{K'}_{37}$ values

205 were converted to temperatures using the calibration for suspended particulate matter (Conte et al., 2006):

$$SST_{UK} (°C) = -\ 0.957 + 54.293\ U^{K'}_{37} -\ 52.894(U^{K'}_{37})^2 + 28.321\ (U^{K'}_{37})^3 \tag{17}$$

A systematic and statistically significant difference between the average SST_{UK} of CBeu1–4 (Mollenhauer et al., 2015) and

210 CBeu5 is observed (t-test for the same mean p = 0.0014; F-test for same variance p= 0.024; Monte Carlo permutation, mean p= 0.0014, variance p = 0.0016 with 10^4 permutations; Epps–Singleton test for the same distribution of two univariate samples p = 1.5 10^{-6}). Correcting of this analytical discrepancy has been performed on the basis that alkenone composition reflects reliably the ambient temperature during production (Conte et al., 2006). Furthermore, we allowed for a small degree of selective degradation during transport through the water column, resulting in slightly higher SST_{UK} (global calibration of

215 $U^{K'}_{37}$ from suspended particulate matter (SPM) to ambient SST (Conte et al., 2006). By subtracting 0.094 $U^{K'}_{37}$ units, the CBeu5 SST_{UK} average equals that of CBeu1–4. Application of the global calibration reveals a deviation of 0.45°C from SST_{SAT} for the entire series CBeu1–5 ($SST_{SAT} = 0.723\ SST_{UK} + 5.56$; φ = 35 days; r^2=0.60, average 21.76°C) and since the slope of the global calibration differs from our dataset, the reconstructed SST_{UK} show an offset of almost +0.8°C from SST_{SAT} at the lower temperatures (18°C) and an offset of -1.9°C at 26°C. Logically, the alternative, a local calibration

220 removes this offset. For details about this correction and the local cubic calibration we refer to supplemental material (Sup. Fig. S3).

2.6 Diatom data

Diatom counting has been performed as described in Romero et al., (2020). Data for *Proboscia alata* are presented here for the first time.

2.7 External data

2.7.1 Insolation (as Heading 3)

Solar insolation at 20°N has been obtained from https://www.pveducation.org/pvcdrom/properties-of-sunlight/calculation-of-solar-insolation. This record provided insolation for each 5th day. The four most important frequency components were extracted using the sum of sinusoids model of PAST4 of the insolation explaining 99.994 % of its variance have been used to generate a 5–years insolation record with daily resolution for comparison with the daily SST_{SAT} record (Fig. 2).

The insolation is not a simple sinus wave, the lowest half of the insolation amplitude (7.777—10.744 W m^{-2} d^{-1}) includes 41.2% of the year (152 d), the highest half accounts for 58.8% (213 d). The 10% highest insolation (>10.447 W m^{-2} d^{-1}) occurs for 28% (103 d) of the year, the 10% lowest insolation values (< 08.074 W m^{-2} d^{-1}) occur at 17% (62d) of the year (Fig. 2a).

2.7.2 Daily sea surface temperatures

Satellite-derived SST_{SAT} values for the CBeu have been obtained from the ERDDAP daily optimum interpolation (OI), AVHRR dataset (Dataset ID: ncdcOisst21Agg_LonPM180) for 20.875N, 18.625W, the grid point closest to the location of CBeu and representing the square enclosed by 21°N, 18.75°W and 20.75°N, 18.5°W (Fig. 1, green square). For each cup, the daily SST_{SAT} values have been averaged (binned) for the respective deployment time (each bin being the interval between the starting and ending dates for each cup deployment). Since it takes time for material produced in the water column to arrive in the cup, the SST_{SAT} have also been calculated for bins shifted by one day (φ = 1) to 140 days (φ = 140) back in time. In this study we assume that φ is constant over time. Since the purpose of the SST proxies is to reconstruct SST, we took the φ that gave the best correlation between the binned SST_{SAT} record and the proxy-based reconstructed SST as collected by the sediment trap.

2.7.3 Monthly subsurface water temperatures, salinity and nutrient data

Subsurface temperatures and salinities were obtained from the World Ocean Atlas 2018 (Locarnini et al., 2018; Zweng et al., 2019) using the statistical mean temperature on a 1° square for all decades centred at 18.5° W, 20.5° N. (Fig. 3). Monthly phosphate data for different water depths have been obtained from the World Ocean Atlas 2018 (Garcia et al., 2019) on a 5° grid point centred at 22.5° N, 17.5° W since insufficient data were available for a 1° grid point).

250 **2.7.4 Wind direction and wind speed**

Wind direction and strength are based on 3 hourly observations from Nouadhibou airport (20° 56′ N, 17° 2′ W; Institut Mauretanien de Recherches Océanographiques et des Pêches, Nouadhibou, Mauritania). Since these data are vector-based (direction and speed) they can't be simply averaged (The average of 1 h 10 m/s at 350° and 1h 10 m/s at 10° is 1h 9.85 m/s at 0° and not 1 h 10 m/s 180°). Therefore, the data have been decomposed into their North–South (V_n) and East–West

255 components (V_e), averaged and converted back to directions and speeds (see Grange 2014 and http://www.webmet.com/met_monitoring/622.html\). Since there is a high variability between the days, 11 days moving averages have been used to reduce this high frequency contribution (Fig. 2). Furthermore, the deviation from north is presented (-90° is west, + 90° east) rather than the full 360° scale).

2.7.5 Dust events

260 The dust data (Fig. 2) represent the monthly number of dust events at Nouadhibou Airport (20°56′N, 17°2′W) and have been obtained from the Institut Mauretanien de Recherches Océanographiques et des Pêches, Nouadhibou, Mauritania (Romero et al., 2020) (Fig. 2f).

2.6 Statistics

Statistical analyses have been performed with the software package PAST4.0.4 (Hammer 2001) and with R packages

265 'grDevices', 'stats', 'EnvStats', 'methods' and 'car'. Phase shifts reported between proxy records and SST_{SAT} represent the phase for which the correlation is highest. Phases are represented by φ, wavelengths by λ.

3 Results

3.1 Environmental data

3.1.1 Daily sea surface temperatures

270 Daily SST_{SAT} are above average (21.3°C) from July to December (5 months) and low and relatively constant from December to July (7 months Fig. 2b). The maximum temperature is reached at Sept 30th (day 273, just over 6 months after the minimum).

The records of binned SST_{SAT} averages (representing the averaged SST for the deployment period of each cup) varies depending on the assumed phase shift (φ) between the genesis of a signal at the sea surface and its arrival in the cup of the

275 sediment trap. Minima lay between 17.9–18.4 °C, maxima between 26.2–27.2 °C and annual amplitudes between 7.8–8.9°C.

3.1.2 Monthly subsurface water temperatures, salinity and nutrients

The temperature–salinity diagram for the upper 600 m (Fig. 3) shows for November–December a predominantly South Atlantic Central Water (SACW) signature with relatively low salinities for a given temperature (or high temperatures for a given salinity). From January, the contribution of North Atlantic Central Waters (NACW) increases. From March to June the
280   upper 80 m show admixture of cool, low salinity waters (but absent in April) so that despite increasing insolation the SST stay below 19°C for this period.

For the upper 40 m a decrease in PO_4^{3-} occurs from January with a minimum in April (Fig. 3). In May June and July the values are back at their February–March values and return to the April minimum from August to October, coinciding with the summer stratification. From September, values increase to the January maximum. Below 40 m, the highest PO_4^{3-} are not
285   in January but in December. Values stay more or less constant from January to May. In June and July they increase and sharply fall to a minimum in August. In September and October values are back to June values and they further increase in November and December.

3.1.3 Wind direction and wind speed

From 2003 to 2008 the 11 days averaged wind blows 87% of the time from NW to NE (36°W — 21°E) and 52% of the time
290   from NNW to NNE (17°W–7°E). Most easterly directions occur in a relatively short period from November to February, when wind speed is at its lowest on average (Fig. 2d). This phase with more westerly winds was poorly developed in 2005/06. This is followed by a period of high wind speeds from March to July with winds more or less constant from the North (or NE in 2006 and 2007; Fig. 2e). A third period, from June to November, has the same overall wind as the preceding period but intercalates more eastward outbreaks and wind speed tends to be lower. Over the investigated period there is an
295   eastward trend (D = -0.0124 d - 7.49, whereby D is the direction in degrees from N and d = Julian day since 01-01-2003; r^2=0.14; p=9.45 10^{-9} n = 1989). This implies that at the beginning of 2003 the average wind direction is 7.5° W and by the end of the study period (after 2000 d) this is 17.4°E. This effect is predominantly due to the years 2007 and 2008 for which from the beginning of May to the end of October the wind has a more easterly direction than during this period in the preceding years (Fig. 2). Frequency analysis shows apart from this long-term trend an annual cycle (363 d) and a 6 months
300   cycle (184.6 d) with its most eastern direction at December 10th.

The 11 days averaged wind speed varies between 1 and 9 m s^{-1} and shows no trend (slope 1.4 10^{-4}). Frequency analysis shows an annual cycle (371 d) and a 6 months cycle (181 d). The phase of the cycle is 45 d (from Jan. 1st) with the maximum wind speed ¼ π later, (45 + 93 = 138 d) which is May 18th.

3.1.4 Dust events

305   The dust record shows a strong seasonal cycle (φ = 55.33 days, λ = 363.2 d) and the abundance of dust events lags wind speed by 10 days.

3.2 Sediment trap mass fluxes and upwelling species abundance

The relative abundance of upwelling species (%Upw) show a clear seasonal cycle and lag wind speed by 21 days (r^2=0.29, p=3.5 10^{-9}) and conversely dust event frequency by 11 days. The %Upw. species correlates well with the SST_{SAT} (negative r^2= 0.53 φ = 76 p<2.5 10^{-20} ; positive r^2=0.40, φ = -119 p < 2 10^{14}). Total mass flux maxima occur in concentrated intervals of which the timing and amplitude may differ between the years. Total mass fluxes, and fluxes of carbonate, C_{org}, biogenic silica and the lithogenic component all closely correlate and are synchronous (e.g. C_{org} Flux = 0.065 *Total Flux +4.20 r^2= 0.74; Fig. 2g,h) (Romero et al., 2020). Maxima may occur at any time but are most frequent in late winter from February to March. In 2003 and 2008 a spring maximum is absent. The years 2005 and 2007 have maxima in late summer. Both the amplitude of the total mass and flux maxima differ between the years. In 2005 a series of small flux maxima occur but a large maximum is missing (**Fig. 2**). As a result of this irregular timing of total mass flux maxima, the most important frequency component is not the annual cycle but a cycle with a length of 257 d (r^2=0.17, p = 4.04 10^{-6}).

3.3 Diol fluxes

The $1,14C_{28}$, $1,14C_{30}$ and $1,15C_{30}$ diols could be detected in 105 of the 120 cups. For several of these cups other diols were below the detection limit with the $1,14C_{30:1}$ detected least, in only 61 cups. Diol flux maxima, coincide with total mass flux maxima (Fig. 2) albeit, not every total mass flux maximum is accompanied by a diol flux maximum. The wavelength of the most important diol flux frequency component is 216 d (r^2=0.14, p < 3.4 10^{-5}). Fluxes of individual diols show a cluster of high correlations consisting of the $1,13C_{30}$ diol and both 1,15 diols (r^2 > 0.75). The $1,13C_{28}$ diol correlates best with the $1,13C_{30}$ diol and (r^2 > 0.75), less with the 1,15 diols (r^2 > 0.50) and even less with the 1,14 diols. The 1,14 diols, correlate best with each other (r^2 > 0.83) whereby the $1,14C_{28}$ diol correlates less with the other diols than $1,14C_{30}$ diol. The $1,14C_{30:1}$ diol does not show strong correlations with the other diols, it correlates best with the $1,14C_{30}$ diol and second with the 1,15 diols. This absence of strong correlations with the $1,14C_{30:1}$ diol we relate to its low concentrations which intrinsically have a large error bar and is accompanied by occurrences below the detection limit. Excluding the $1,14C_{30:1}$ diol, the $1,13C_{28}$ and $1,14C_{28}$ diols correlate least. Thus, overall, the 14 and 15 diols correlate least (r^2 = 0.45), the 13 diols are intermediate but correlate better with the 15 diols (r^2 = 0.79) than the 14 diols (r^2 = 0.48).

3.4 Diol ratios and indices

The productivity related NDI, DI_W, DI_R, DSI and CDI all largely depend on the same diol isomers and except for some DSI relations covary to a considerable extent (r^2 > 0.46; Table 4, Fig. 4). Due to their annual cyclicity, their statistical relations to environment encompass usually two maxima of correlation of opposite sign and about 181 days apart (½ cycle). For some indices the causal relation to environment isn't clear a priori. In case of a negative correlation with environment the correlation is positive if shifted by ½ cycle but this is also true for the unshifted reciprocal of the proxy. Below we often

provide both and negative correlations and their phases with environmental variables without further interpretation which will be added in the discussion.

3.4.1 Temperature proxies LDI, DSI and DCI

340   The SST_{LDI} maximum of 26.7°C is 1.1°C above the binned SST_{SAT} maximum (25.6°C at φ = 41 d, **Fig. 5**). However the minimum of 10.9°C is 7.7°C lower than the lowest binned SST_{SAT} value (18.6°C at φ = 41). In total there are four values below this lowest binned SST_{SAT} and they occur in July 2003, July 2006, and March 2007, all in cup series CBeu1–4. A simple box plot shows that these values are outside the notches which indicate approximately the 95% confidence interval (Fig. 6). The Rossner's Test for identifying multiple outliers (from R–package EnvStats) identifies the lowest four values (<

345   18°C), as outliers (p < 0.006, and for the lowest value <11°C p<0.0001). Cross correlation plots (Fig. 7) of the log transformed diol fluxes shows that the anomalies are most pronounced in the $1,13C_{30}$ diol relative to each of the 1,15 diols and do not correlate with the flux amplitude. For several samples no 1,13 diols could be detected. This lack of information automatically results in LDI values of 1, translating into 27.42°C which is unrealistic in this setting. For these reasons, such data points have been omitted.

350   A linear correlation of LDI to binned SST_{SAT} explains 17% of the variance (φ = 41; p= 1.4 10^{-4} n=82, Table 4). The linear correlation of SST_{LDI} to binned SST_{SAT} also explains only 17% of the SST_{SAT} variance (φ = 38; p=1.2 10^{-4}). The integrated production temperature is 23.6°C (with the outliers 22.9°C).

The DCI correlates significantly with SST_{SAT} (negative correlation at φ =117, r^2=0.35, p<4 10^{-11} positive correlation at φ =-77, r^2=0.29, p<2.8 10^{-9}; Fig. 5). As such SST_{SAT} could be reconstructed from DCI using the positive correlation:

355

SST_{SAT} = 6.45 DCI + 18.4 (95% conf.: slope 4.31 to 8.68, intercept 17.5 to 19.2)   (18)

or the negative correlation:

360   SST_{SAT} = -8.13 DCI + 16.79 (95% conf.: slope -9.99 to -6.12, intercept 23.9 to 25.8)   (19)

The DCI lags wind strength (φ = 30 positive correlation, r^2 = 0.29, p<5.5 10^{-9}). The DCI shares most variance with the NDI (74%) with a negative correlation.

      The DSI correlates strongly with the NDI and DCI (Table 4). The positive correlation with SST_{SAT} (r^2= 0.25, φ = 77

365   p=5.7 10^{-5}) is much lower than the negative correlation (r^2= 0.42, φ = -124 p=3.4 10^{-8}). For a considerable number of samples no unsaturated diols could be detected, these samples were omitted from the calculations.

3.4.2 Upwelling and upper ocean productivity proxies DIR, DIW and CDI

The DI_R, as a proxy for the *Proboscia* contribution shows correlates significantly with the ln *P. alata* flux ($r^2 = 0.29$, p = 1.6 10^{-4}) but not with the total mass flux or its logarithm (Fig. 7).

370   The DI_W as a proxy for upwelling, correlates significantly with the ln *P. alata* flux ($r^2 = 0.12$; p = 0.024) but not with the total mass flux ($r^2 = 0.011$, p = 0.25). The correlation of the DI_w with the LDI is negative low ($r^2=0.04$) and barely significant (p=0.09), for the DI_r and LDI the correlation is also negative but much better ($r^2=0.24$ p=6.3 10^{-7}). Both the DI_R and DI_W show a negative correlation with wind strength which is best at φ = 79 (Table 4).

The Combined Diol Index (Rampen et al., 2014a) CDI, is almost identical to the DI_R ($r^2=0.995$) and therefore has not been
375   evaluated separately.

3.4.3 Upper ocean nitrate and phosphate concentration proxy NDI

The NDI, shares about half its variance with the CDI, DI_W and DI_R, even higher with the DCI (74%) and DSI (67%). The NDI shows no correlation with *P. alata* flux ($r^2=0.005$, p=0.6) nor with the total mass flux ($r^2=0.0014$, p=0.7) but correlates well ($r^2= 0.38$ p=4.1 10^{-12}) with the relative abundance of upwelling indicating species (%Upw) in the samples.

380   ## 3.5 Alkenone based $U^{K'}_{37}$ and SST_{UK}

The SST_{UK} values are 18.0 – 26.1°C and best fit to SST_{SAT} if SST_{UK} at φ = 35 days (Fig. 5). For this phase lag the binned SST_{SAT} are 18.5–26.1°C and the SST_{UK} record thus has about the same amplitude extending 0.5°C below the minimum and equalling the maximum SST_{SAT}. The measured $U^{K'}_{37}$ explains 59% of the SST_{SAT} variance and the SST_{UK} 60%. The integrated production temperature (flux corrected) = 21.14°C, nearly the SST_{SAT} for φ = 35 (21.37°C).

385   The regressions of $U^{K'}_{37}$ and SST_{UK} to binned SST_{SAT} do not differ much in the explained variance and phase (φ 35 d, r^2 =0.59 *vs* 0.60). The flux corrected SST_{UK} for CBeu1–5 prior to correction is 21.54, after correction it 21.14°C which is only 0.23°C lower than the SST_{SAT} for the same period (21.37 φ=35) and well within the standard error of the method (1.2°C) (Conte et al., 2006).

4 Discussion

390   ## 4.1 Water temperatures during the sampling period

During the entire record, SST_{SAT} tend to remain relatively constant for periods of one to three weeks with rapid shifts of 1–2°C between them (Fig. 2). During summer these shifts tend to be larger and they may be up to 4.5 °C within a week at the transitions between summer and winter (in 2004). The length of these 1–3 weeks periods of stable temperatures is similar to the duration of cup deployment (8–24 days) so that these periods are partly reflected by, and consistent features of the binned

395   SST_{SAT} record, irrespective of the phase difference between the SST_{SAT} binned averages and the corresponding cup deployment times. This is much more apparent after November 2006 when the cup deployment is systematically less than 10 days and close to the duration of the shorter-term events of the system. This demonstrates that to capture the systems dynamics, these shorter deployment times are the preferred mode of operation, if not a requirement.

The SST_{SAT} does not simply follow the insolation curve, but a substantial rise in temperature only starts from the beginning
400   of June, only a few weeks before the insolation maximum. We attribute the delay to maximum intensity of the trade winds during late winter and spring, intensifying upwelling and pumping cool, low salinity and nutrient-rich SACW waters to the surface along the coast and subsequently spread these westward over the trap site. Wind speeds are strongly reduced and upwelling is at a minimum for July to October, enabling the surface waters to strongly increase in temperature. The temperature gradient is always small for the upper 20 m, the permanently mixed layer.

405   The most prominent feature of the monthly water temperature profiles is the strong annual cycle at the sea surface which becomes smaller with increasing depth. In the upper 100 m the relatively short distances between the temperature profiles for different depths (the strength of the temperature gradient) are clearly smaller from January to June compared to the rest of the year. We attribute this to mixing and upwelling. This seems to be most intense in May and June. In May this is indicated by elevated temperatures up to 400 m depth and in June the upwelling and mixing result in SST that are even lower than the
410   preceding months, despite stronger solar insolation. We also observe that the highest temperatures at depth (80–200m) lead the SST by about three months (Fig. 3) which in case of temperature proxies generated at these depths could lead to proxy-derived temperature records leading SST.

4.2 The annual cycle, wind, dust SST and upwelling

All environmental parameters investigated show a dominant annual cycle modulated by a semi-annual component. This is
415   also true for most of the proxy records. This implies that a significant correlation of a proxy parameter to an environmental variable, with a given phase shift has a high chance to also provide significant correlations with other environmental parameters, albeit with different phase relations. This is no problem for proxy records that are well investigated and relatively well understood, such as the $U^{K'}_{37}$ for which we know a causal relation with temperature. However, for several of the diol-based records only statistical correlations are known and causal mechanistic understanding of the relations to
420   environment are largely absent. Due to the cyclic nature of data, a proxy record has two correlation optima per cycle. One optimum is a positive correlation, the next optimum is an anti-correlation, located ½ cycle distance from the first optimum, if the cycle is perfectly sinusoid. If we don't know the proxy–environment relation, this second, antic-correlation can also be seen as a positive correlation with the inverse (B/A in stead of A/B) of the proxy and since the relation is statistical rather than causal, there is no a priori argument against considering the reciprocal of the proxy as the better one relating to
425   environmental change. Additional arguments, e.g., from the data structure and/or functioning of the system are needed to decide if the proxy or its reciprocal is the better one. In our system, off Cap Blanc, the modulation of the semi-annual

frequency component causes asymmetry in the cycles of the environmental variables (Fig. 2). As a result, phases of best correlation and anti-correlation are not ½ cycle apart. Comparison of wind speeds and SST_{SAT} in this region shows that both have a short period of high values, followed by a relatively long period of low values. If proxy records follow environmental

430 change closely, they also should display this asymmetry in the annual cycle. High wind speeds in late winter and spring drive upwelling, preventing SST_{SAT} to increase with solar insolation so that only when wind ceases by the beginning of June, SST_{SAT} can rapidly rise. This results in maximum wind speed leading maximum SST by 122 days (based on 11 day means, $r^2=0.38$) and minimum SST leading maximum wind speed by 91 days ($r^2=0.37$). The asymmetry in the annual cycle thus leads to an alternation of 122+91=213 day difference between correlation optima, followed by a 365-213=152 day difference

435 between the next correlation optima. We expect to see this asymmetry also in the proxy records. The frequency of dust events lags wind speed by 10 days so that most events occur during the period of most active upwelling. Due to this small phase difference in relation to the generally two to three times longer sample frequency of the sediment traps it is impossible to separate the effects of upwelling and dust input on the export flux, species and lipid composition. Since wind speed is driving both upwelling and dust event frequency, only relations to wind speed are further considered.

440 **4.3 Diol based temperature proxies LDI, DSI and DCI**

The LDI uses the underlying assumption that the percentages of 1,13 diols (relative to the $1,15C_{30}$ diol) decrease with temperature. For the SST_{LDI} outliers (values below 18°C) we couldn't find any analytical explanation. These outliers arise from excess production of both 1,13 diols. The occurrence of these anomalies suggests that this excess production is unrelated to temperature. We observe that all three events with excess 1,13 diols (and very low LDI values) occur during

445 Total Flux maxima (compare Figs. 5, 9) and as such we speculatively suggest that factors leading to elevated export productivity play a role. However, also with the outliers omitted, we observe a poor relationship between LDI and SST_{SAT} and a phase lag of 41 days ($r^2=0.17$) but still a significant seasonal cycle ($\lambda=347$ d, $r^2=0.36$, p=1.2 10^{-10}). This contrasts with trap studies from the equatorial Atlantic, Mozambique Channel and to a lesser extent the Cariaco Basin where a general absence of a seasonal cycle in the LDI has been observed (de Bar et al., 2019). The SST_{LDI} integrated production temperature

450 (23.6°C) is well above the annual SST_{SAT} (21.3°C). This may be explained by the general observation that 1,13 and 1,15 diol production is weighted towards the non-upwelling season, which has above average temperatures (as is also indicated by the poor correlation of 1,15 and 1,13 diols with 1,14 diols Fig. 7).

The LDI shows strong covariance with DSI and DCI. Since these proxies are based on completely different diols (LDI 1,15 and 1,13 diols, DSI and DCI 1.14 diols) this covariance has thus no mathematical basis but rather should be sought in

455 common sources or responses to environmental change.

Due to the partial absence of detected unsaturated diols, valid values of the saturation index DSI could be calculated for only half of the samples. Application of the culture-based transfer function to these samples provides unrealistic water temperatures for the CBeu surface waters (range 10.1–41.0°C, average 33.2°C) and this transfer function is thus not

applicable to this region. The DSI, lags SST_{SAT} (r^2= 0.25, φ = 76, n=58) which is a much longer time span than observed for
460   the LDI (φ = 41). This difference may indicate that sinking speed of the 1,14 diols (comprising the DSI) differs from that of
the 1,13 and 1,15 diols (comprising the LDI). It may also be that changes in the 1,14 diol composition represent an
environmental response different from the response changing the 1,13 and 1,15 diols composition. One explanation may be
that the 1,14 diols are produced by different organisms than the 1,13 and 1,15 diols, which allows for both different sinking
speeds and different environmental responses. In the marine environment the 1,13 and 1,15 diols are considered to be
465   predominantly derived from marine eustigmatophytes (e.g. Gelin et al., 1997; Volkman et al., 1992, 1999; Versteegh et al.,
2000; Rampen et al., 2014b). The 1,14C_{32} diol is a major diol in the diatom *Apedinella radians* (Rampen et al., 2011) but
since we do not observe this diol in our cup samples, we infer that this species doesn't significantly contribute diols in our
case. In our samples we do observe a relative good correlation between fluxes of the diatom *Proboscia alata* with the 1,14
diols (31% explained variance, Fig. 8). This correlation is considerably better than the correlation between *P. alata* fluxes
470   and 1,13+1,15 diols (4%) or between total diatoms and 1,14 diols (17%). This suggests that *Proboscia* significantly
contributes 1,14 diols whereas its 1,13+1,15 diol contribution is insignificant. Culture experiments demonstrate this ability
for *P. alata* to produce 1,14 diols (Sinninghe Damsté et al., 2003). Our observations also agree well with diol data from
sediment traps from the Arabian Sea where abundance of 1,14 diols covaries with upwelling and appears unrelated to the
abundance of 1,15 diols (Rampen et al., 2007). Also a recent sediment trap study from the East Sea (Gal et al., 2021)
475   supports the hypothesis of 1,14 diols being produced by a different plankton population than the 1,13 and 1,15 diols. In these
sediment traps (March 2011–March 2012) the 1,14 diols show very similar and temporally narrowly confined flux maxima
in Oct. and Nov. 2011 whereas the 1,13 and 1,15 diols show a very different pattern with broader flux peaks and almost
permanent presence.

Assuming the upwelling related *Proboscia* diatoms being a major 1,14 diol source in our research area, it makes sense to
480   investigate if and how the DSI relates to wind induced upwelling and %Upw. During the investigated time interval, SST_{SAT}
lags wind speed by about one season (φ =122 r^2=0.342). With diatom sinking rates in this region of 100 – 250 m d^{-1} (Fischer
and Karakaş 2009) and 1280 m trap depth, particles are expected to arrive at the trap within 5–12 days after starting to sink.
We observe that the abundance of upwelling species (%Upw) lags wind speed by 21 days (r^2=0.26, p=6.8 10^{-9}) agreeing
reasonably well with the estimated sinking speed (Romero et al., 2020). We therefore expect the DSI to behave similar to the
485   %Upw lagging the wind speed by 21 days and leading SST_{SAT} by 101 days. We observe the DSI lags the SST_{SAT} by 76 days
and is not leading it as was assumed based on the arguments above. However, the inverse DSI (higher values more diol
unsaturation) provide a completely different picture lagging wind speed with the same phase (φ = 21, r^2=0.24 p=9.7 10^{-5}) and
correlates well with %Upw (r^2=0.39). It also correlates surprisingly well with SST_{SAT} leading it by 124 days (φ=-124, r^2=0.
42). We therefore, propose that the inverse DSI reflects upwelling related changes with a higher contribution of unsaturated
490   diols upon stronger upwelling. Interestingly, also in the East Sea sediment trap (Gal et al., 2021) the 1,14$C_{28:1}$ is the only diol
involved in the diol flux maximum in spring 2011 whereas all 1,14 diols are involved in the narrow diol flux peak in autumn
2011. Both these spring and autumn diol maxima occur during productivity maxima which also show maxima of diatom

export production (Kim et al., 2017). Gal et al. (2021) ascribe the spring $1,14C_{28:1}$ diol maximum to *P. alata* whereas they relate the autumn maximum including also the $1,14C_{30}$ diols to *P. indica,* a species absent from Cap Blanc. The DSI thus

495 seems to be heavily modulated by processes related to high productivity obscuring a possible relation to water temperature, if present.

The DCI leads the SST_{SAT} (φ=-77, r^2=0.29). Since the reconstructed SST can't precede the actual SST, it is unlikely that the DCI reflects SST. Moreover, available transfer functions (see Methods 3.4) lead to unrealistic temperatures for CBeu. The inverse of the DCI lags SST (best correlation r^2=0.35 at φ=117) but simultaneously its average chain length

500 decreases with temperature, which is opposite to the common physiological response of organisms to temperature (higher lipid melting point/viscosity at higher temperatures). Consequently, a causal relation through physiological adaptation of the diol-producing organisms to SST must be considered unlikely.

The DCI follows wind speed by 27-31 days (r^2=0.28, φ=27, p= 7.5 10^{-9}; φ=31, p=6.4 10^{-9}) and upwelling species (%Upw) by 6–9 days (r^2=0.42). This suggests that like the DSI, also the DCI reflects changes in the upwelling regime. Interestingly, both

505 these supposedly upwelling related DSI and the DCI correlate better to SST_{SAT} than the temperature proxy LDI which we attribute to the (annual) cyclic nature of the system rather than to a causal relation with temperature.

4.4 Diol based productivity/nutrient concentration proxies NDI, DIR, DIW, and CDI

4.4.1 NDI

The NDI, DSI and DCI correlate well (r^2>0.68). This is expected since although the NDI consists of all diols encountered, it

510 combines the DSI and inverse DCI. The 1,14 diols in these two latter proxies obviously dominate the NDI. The NDI has been proposed to reflect NO_3^- and PO_4^{3-} concentrations in the surface waters (Gal et al., 2018, 2019, 2021). If in our setting, we assume that upwelling and the relative abundance of upwelling species (%Upw) are associated with nutrient-rich conditions at the CBeu site, a significant positive correlation between NDI and %Upw is expected. However, our results show a negative correlation (Table 4). The interpretation of the NDI as reflecting NO_3^- and PO_4^{3-} concentrations in the

515 surface waters is further complicated by a clear annual cycle in our dataset whereas monthly PO_4^{3-} and NO_3^- concentrations show no cyclicity. Furthermore, mostly concentrations of these nutrients show no correlation with the NDI (p <0.04).

A closer look at the NDI reveals that, the slopes of the respective transfer functions relate to each other according to the Redfield Ratio N:P = 16:1. This may be expected since the original calibration between NDI and nutrients (Gal et al., 2018) is primarily based on sediment-derived NDI values and photic zone annual nutrient levels (n=216), the latter following the

520 Redfield ratio. SPM summer samples with associated summer nutrient concentrations are also included in this Gal et al. (2018) sediment–sea surface dataset. The NDI–PO_4^{3-} relation of these SPM samples falls within that of the sediment samples but, for the SPM samples alone, correlation with the PO_4^{3-} concentrations is not significant (r^2=0.2, p=0.14). A sediment trap study from the East Sea (Gal et al., 2021), shows a different relation between the trap NDI values and monthly sea surface PO_4^{3-} concentrations (r^2=0.59, n=26). In the East Sea, PO_4^{3-} concentrations and NDI show a clear annual cycle. However,

525 this is true for most environmental parameters, and it would be interesting to see what part of the observed correlation between NDI and PO_4^{3-} is causal and what part results from a common (annually cyclic) forcing factor.

4.4.2 DI_W, DI_R and CDI

The DI_w, DI_R and CDI have the same 1,14 diols in the numerator and only differ in the combination of 1,13 and 1,15 diols in the denominator. The CDI only adds the $1,15C_{30}$ diol to the DI_R. The DI_w has been directed as a proxy for the contribution of

530 *Proboscia* diols relative to other diols. In our dataset, its correlation with the *Proboscia* fluxes is low but still significant (r^2=0.12 p=0.024). The proxies for upwelling strength DI_R and CDI correlate even better with *Proboscia* (Table 4).

The DI_R has been suggested to be proxy reflecting total export productivity. We observe high values (>0.9) of this proxy which would indicate a permanent high production in the region. Both the DI_W and DI_R correlate negatively with wind speed (at φ = 79) and SST_{SAT} (at φ = -69). Closer observation shows that generally, all diol fluxes more or less covary except in

535 2007 where pulses in 1,13 and 1,15 diols precede those of the 1,14 diols (Fig. 9) and the DI_R sinks below 0.8. Comparison to the total mass flux (correlation insignificant) and to the %Upw reveals that this change in diol composition is not accompanied by a consistent change in export flux so that an explanation for the relative increase in 1,15 diols seems to require a more subtle knowledge of the relation between diol abundance and environment on the CBeu trap data alone.

Other trap studies reporting diol fluxes from tropical Atlantic are upper traps from 1150 m depth in the Eastern Atlantic near

540 the Guinea Dome and influenced by seasonal upwelling (M1U), from 1235 m depth in the oligotrophic Central Atlantic (M2U) and from 1130 m depth in the western Atlantic and under seasonal influence from the Amazon outflow (M4U) (de Bar 2019). It appears that for the 1,13+1,15 diols our average of 3.9 μg $m^{-2}d^{-1}$ for CBeu5 is only 1.5 times the average for the nearest trap M1U (2.6 μg $m^{-2}d^{-1}$), and about 3 times the flux of the oligotrophic central Atlantic M2U (1.2 μg $m^{-2}d^{-1}$) but only half that of the westernmost M4U (7 μg $m^{-2}d^{-1}$). For the 1,14 diols the average of 1.7 μg $m^{-2}d^{-1}$ for CBeu5 is least three times

545 higher than for the other traps (0.5 for M1U, 0.01 for M2U and 0.3 for M4U). Since CBeu5 is the only site under permanent upwelling influence, we infer that the 1,14 diols are particularly abundant in the (coastal) upwelling whereas the 1,13 and 1,15 diols also increase with increasing productivity but seem to be less bound to upwelling.

4.5 $U^{K'}_{37}$ and SST_{UK}

The 35 days phase lag of SST_{UK} relative to SST_{SAT} suggests that it takes about one month between fixation of the alkenone

550 composition in the cell and the collection of the alkenones in the cup of the sediment trap which implies an average sinking rate of 38 m d^{-1}.

This differs strongly between the years. From winter to summer 2007 both SST records nicely overlap, suggesting a much higher sinking rate, also in the following autumn and winter 2003/2004 and 2005/2006 this is less than 15 m d^{-1}.

The complex cubic transformation of $U^{K'}_{37}$ values to SST_{UK} for SPM derived from a global dataset (Conte 2006) doesn't

555 correlate better than $U^{K'}_{37}$ itself. This implies that in this case a linear transformation would have performed equally well.

This we may expect since our data cover only a fraction (18–27°C) of the global temperature range and for this fraction the cubic transformation behaves almost linear. Since the explained variance is much lower (60%) than for the global calibration (97%) we infer that other factors than temperature influence the alkenone composition. If the reconstructed SST_{UK} would perfectly project to the SST_{SAT} the slope of the regression would be 1 and the intercept 0. However, the slope of the SST_{UK}

560 regression to binned SST_{SAT} is 0.72 and the intercept 5.6, which implies that the global SPM calibration overestimates local SST_{SAT} below 20°C and underestimates local values above this temperature. If we assume that the global calibration is correct and the alkenones reflect the water temperature the organisms were subject to, the conclusion would be that above 20°C the organisms live in water that is slightly cooler than that at the sea surface (SST_{SAT}) and slightly warmer below this temperature. This could be explained by a higher influence of solar irradiation at the sea surface than at the subsurface. This

565 is only feasible if the alkenone-producing organisms live partly or entirely below the surface mixed layer. Alternatively, we may adjust the SPM calibration of Conte et al. (2006) such that we obtain a local calibration where the slope and intercept agree with the binned SST_{SAT} data (φ = 35) providing (see also supplementary Fig. S3):

$$SST_{UK}\ (°C) = 0.64733 + 54.293\ U^{K'}_{37} - 52.894(U^{K'}_{37})^2 + 23.382\ (U^{K'}_{37})^3 \tag{20}$$

570

with φ = 33 and r^2=0.54. Just like the global calibration of Conte et al. (2006) this regional calibration performs much better than any of the diol proxies discussed above.

5 Conclusions

The variation in alkenone, and diol, fluxes and relative abundances as observed in sediment trap cups off Mauritania from

575 2003 to 2008 have been compared with environmental conditions and plankton composition for the same region and time period. From this comparison, it appears that:

1. Peak total mass fluxes of material to the sediment trap do not show a statistically significant annual cycle but may occur throughout the year. Nevertheless, total mass flux maxima are most abundant during spring. We explain this rather unpredictable occurrence of these flux maxima by attributing them to result from the passage of upwelling filaments over the

580 sediment trap which occurs most often during spring, but is not limited to this.

2. Off Cap Blanc, upwelling variability is the major environmental variable. It shows a strong annual cycle in response to the strength of the trade winds. Sea surface temperature also shows a strong annual cycle remaining low in winter and during vernal upwelling and following insolation when upwelling is reduced during summer. It lags upwelling by 130 days. As a result of the predominant annual cycle in both temperature and upwelling, correlations between parameters and/or proxy

585 records should be interpreted with care and phase relations should be considered to identify the most likely forcing mechanism.

3. The alkenone-based $U^{K'}_{37}$ lags SST by 35 days and excellently reconstructs both SST with respect to amplitude and absolute values.

4. The diol derived LDI lags SST by 40 days. It correlates only weakly with SST and shows several outliers to very low 590 reconstructed temperatures.

5. The diol-derived nutrient index NDI, the DCI as well as the percentage of upwelling species correlate better with SST than the LDI. However, they lead the SST by several months and their variability is most likely a response to upwelling associated processes rather than temperature. A rather intriguing result is the anti-correlation between the diol-derived nutrient proxy NDI and upwelling intensity.

595 **6 Code availability**

Not applicable

7 Data availability

Data are available at https://doi.org/10.1594/PANGAEA.xxxxx (Versteegh et al., 202X).

8 Author contribution

600 GJMV interpreted the data and wrote most of the manuscript. KAFZ discussed and edited the paper prior to submission. JH processed performed the lipid analyses of CBeu5 and contributed to the Material and Methods section. OER contributed the diatom data and together with GM critically reviewed earlier versions of the manuscript. GF coordinated the sediment trap project.

8 Competing interests

605 The authors declare that they have no conflict of interest.

9 Disclaimer

Publisher's note: Copernicus Publications remains neutral with regard to jurisdictional claims in published maps and institutional affiliations.

10 Acknowledgements

610 We thank Eleonora Uliana for measuring the diol data of CBeu1–4 and Enno Schefuss for constructive comments on an earlier version of the manuscript. We thank N.N. and N.N. for their constructive reviews.

11 Financial support

This research has been financially supported by the German Science Foundation (DFG) through grant GZ:EXC 2077/1 Further financial support was obtained from the Helmholtz Association (Alfred Wegener Institute Helmholtz Centre for
615 Polar and Marine Research). The article processing charges for this open-access publication were covered by Brememn University

12 Review statement

This paper was edited by N.N. and reviewed by N.N. and N.N.

References

620 Balzano, S., Lattaud, J., Villanueva, L., Rampen, S. W., Brussaard, C. P. D., Bleijswijk, J. van, Bale, N., Sinninghe Damsté, J. S., and Schouten, S.: A quest for the biological sources of long chain alkyl diols in the western tropical North Atlantic Ocean, 15, 5951–5968, https://doi.org/10.5194/bg-15-5951-2018, 2018.

de Bar, M. W., Ullgren, J. E., Thunnell, R. C., Wakeham, S. G., Brummer, G.-J. A., Stuut, J.-B. W., Sinninghe Damsté, J. S., and Schouten, S.: Long-chain diols in settling particles in tropical oceans: insights into sources, seasonality and proxies, 16,
625 1705–1727, https://doi.org/10.5194/bg-16-1705-2019, 2019.

de Bar, M. W., Weiss, G., Yildiz, C., Rampen, S. W., Lattaud, J., Bale, N. J., Mienis, F., Brummer, G.-J., Schulz, H., Ruch, D., Kim, J.-H., Donner, B., Knies, J., Lückge, A., Stuut, J.-B., Sinninghe Damsté, J. S., and Schouten, S.: Global temperature calibration of the Long chain Diol Index in marine surface sediments, 142, 103983, https://doi.org/10.1016/j.orggeochem.2020.103983, 2020.

630 Basse, A., Zhu, C., Versteegh, G. J. M., Fischer, G., Hinrichs, K.-U., and Mollenhauer, G.: Distribution of intact and core tetraether lipids in water column profiles of suspended particulate matter off Cape Blanc, NW Africa, 72, 1–13, https://doi.org/10.1016/j.orggeochem.2014.04.007, 2014.

Brassell, S. C., Eglinton, G., Marlowe, I. T., Pflaumann, U., and Sarnthein, M.: Molecular stratigraphy: a new tool for climatic assessment, 320, 129–133, 1986.

635 Chavez, F. P. and Messié, M.: A comparison of eastern boundary upwelling ecosystems, Progress in Oceanography, 83, 80–96, https://doi.org/10.1016/j.pocean.2009.07.032, 2009.

Conte, M. H., Thompson, A., Lesley, D., and Harris, R. P.: Genetic and physiological influences on the alkenone/alkenoate versus growth temperature relationship in *Emiliania huxleyi* and *Gephyrocapsa oceanica*, 62, 51–68, 1998.

Conte, M. H., Sicre, M. A., Rühlemann, C., Weber, J. C., Schulte, S., Schulz–Bull, D., and Blanz, T.: Global temperature
640   calibration of the alkenone unsaturation index ($U^{K'}_{37}$) in surface waters and comparison with surface sediments, 7, Q02005, https://doi.org/10.1029/2005GC001054, 2006.

Cropper, T. E., Hanna, E., and Bigg, G. R.: Spatial and temporal seasonal trends in coastal upwelling off Northwest Africa, 1981–2012, 86, 94–111, https://doi.org/10.1016/j.dsr.2014.01.007, 2014.

Fischer, G. and Karakaş, G.: Sinking rates and ballast composition of particles in the Atlantic Ocean. Implications for the
645   organic carbon fluxes to the deep ocean, 6, 1–18, 2009.

Gabric, A. J., Garcia, L., Camp, L. V., Nykjaer, L., Eifler, W., and Schrimpf, W.: Offshore export of shelf production in the Cape Blanc (Mauritania) giant filament as derived from coastal zone color scanner imagery, 98, 4697–4712, https://doi.org/10.1029/92JC01714, 1993.

Gal, J.-K., Kim, J.-H., and Shin, K.-H.: Distribution of long chain alkyl diols along a south-north transect of the northwestern
650   Pacific   region: Insights   into   a   paleo   sea   surface   nutrient   proxy,   119,   80–90, https://doi.org/10.1016/j.orggeochem.2018.01.010, 2018.

Gal, J.-K., Kim, J.-H., Kim, S., Lee, S. H., Yoo, K.-C., and Shin, K.-H.: Application of the newly developed nutrient diol index (NDI) as a sea surface nutrient proxy in the East Sea for the last 240 years, 503, 146–152, https://doi.org/10.1016/j.quaint.2018.11.003, 2019.

655   Gal, J.-K., Kim, J.-H., Kim, S., Hwang, J., and Shin, K.-H.: Assessment of the nutrient diol index (NDI) as a sea surface nutrient proxy using sinking particles in the East Sea, 231, 103937, https://doi.org/10.1016/j.marchem.2021.103937, 2021.

Garcia, H. E., Weathers, K., Paver, C. R., Smolyar, I., Boyer, T. P., Locarnini, M. M., Zweng, M. M., Mishonov, A. V., Baranova, O. K., Seidov, D., and Reagan, J. R.: World Ocean Atlas 2018. Vol. 4: Dissolved Inorganic Nutrients (phosphate, nitrate and nitrate+nitrite, silicate), 35, 2019.

660   Gelin, F., Volkman, J. K., de Leeuw, J. W., and Sinninghe Damsté, J. S.: Mid-chain hydroxy long-chain fatty acids in microalgae from the genus *Nannochloropsis*, 45, 641–646, https://doi.org/10.1016/S0031-9422(97)00068-X, 1997.

Grange, S. K.: Technical note: Averaging wind speeds and directions, https://doi.org/10.13140/RG.2.1.3349.2006, 2014.

Hammer, Ø., Harper, D. A. T., and Ryan, P. D.: PAST: Paleontological statistics software package for education and data analysis, 4, 1–9, 2001.

665   Ho, S. L. and Laepple, T.: Flat meridional temperature gradient in the early Eocene in the subsurface rather than surface ocean, 9, 606–610, https://doi.org/10.1038/NGEO2763, 2016.

Kim, M., Hwang, J., Rho, T., Lee, T., Kang, D.-J., Chang, K.-I., Noh, S., Joo, H., Kwak, J. H., Kang, C.-K., and Kim, K.-R.: Biogeochemical properties of sinking particles in the southwestern part of the East Sea (Japan Sea), Journal of Marine Systems, 167, 33–42, https://doi.org/10.1016/j.jmarsys.2016.11.001, 2017.

670 Kremling, K., Lentz, U., Zeitzschel, B., Schulz-Bull, D. E., and Duinker, J. C.: New type of time-series sediment trap for the reliable collection of inorganic and organic trace chemical substances, 67, 4360, https://doi.org/10.1063/1.1147582, 1998.

Lathuilière, C., Echevin, V., and Lévy, M.: Seasonal and intraseasonal surface chlorophyll-a variability along the northwest African coast, J. Geophys. Res., 113, C05007, https://doi.org/10.1029/2007JC004433, 2008.

Lattaud, J., Dorhout, D., Schulz, H., Castañeda, I. S., Schefuß, E., Sinninghe Damsté, J. S., and Schouten, S.: The C_{32}

675 alkane-1,15-diol as a proxy of late Quaternary riverine input in coastal margins, 13, 1049–1061, https://doi.org/10.5194/cp-13-1049-2017, 2017a.

Lattaud, J., Kim, J.-H., De Jonge, C., Zell, C., Sinninghe Damsté, J. S., and Schouten, S.: The C_{32} alkane-1,15-diol as a tracer for riverine input in coastal seas, 202, 146–158, https://doi.org/10.1016/j.gca.2016.12.030, 2017b.

de Leeuw, J. W., Rijpstra, W. I. C., and Schenck, P. A.: The occurrence and identification of C_{30}, C_{31} and C_{32} alkan-1,15-

680 diols and alkan-15-on-1-ols in Unit I and Unit II Black Sea sediments, 45, 2281–2285, 1981.

Locarnini, M. M., Mishonov, A. V., Baranova, O. K., Boyer, T. P., Zweng, M. M., Garcia, H. E., Reagan, J. R., Seidov, D., Weathers, K., Paver, C. R., and Smolyar, I.: World ocean atlas 2018, Vol 1: Temperature, 2018.

Lovecchio, E., Gruber, N., Münnich, M., and Lachkar, Z.: On the long-range offshore transport of organic carbon from the Canary Upwelling System to the open North Atlantic, 14, 3337–3369, https://doi.org/10.5194/bg-14-3337-2017, 2017.

685 Lovecchio, E., Gruber, N., and Münnich, M.: Mesoscale contribution to the long-range offshore transport of organic carbon from the Canary Upwelling System to the open North Atlantic, 15, 5061–5091, https://doi.org/10.5194/bg-15-5061-2018, 2018.

Mollenhauer, G., Basse, A., Kim, J.-H., Sinninghe Damsté, J. S., and Fischer, G.: A four-year record of $U^{K'}_{37}$- and TEX_{86}-derived sea surface temperature estimates from sinking particles in the filamentous upwelling region off Cape Blanc,

690 Mauritania, 97, 67–79, https://doi.org/10.1016/j.dsr.2014.11.015, 2015.

Müller, P. J., Kirst, G., Ruhland, G., Von Storch, I., and Rosell-Melé, A.: Calibration of the alkenone paleotemperature index based on coretops from the eastern South Atlantic and global ocean (60°N–60°S), 62, 1757–1772, 1998.

Prahl, F. G. and Wakeham, S. G.: Calibration of unsaturation patterns in long-chain ketone compositions for palaeotemperature assessment, 330, 367–369, 1987.

695 Rampen, S. W., Schouten, S., Koning, E., Brummer, G.-J. A., and Sinninghe Damsté, J. S.: A 90 kyr upwelling record from the northwestern Indian Ocean using a novel long-chain diol index, 276, 207–213, https://doi.org/10.1016/j.epsl.2008.09.022, 2008.

Rampen, S. W., Schouten, S., Schefuß, E., and Sinninghe Damsté, J. S.: Impact of temperature on long chain diol and mid-chain hydroxy methyl alkanoate composition in *Proboscia* diatoms: Results from culture and field studies, 40, 1124–1131,

700 https://doi.org/10.1016/j.orggeochem.2009.08.005, 2009.

Rampen, S. W., Willmott, V., Kim, J.-H., Uliana, E., Mollenhauer, G., Schefuß, E., Sinninghe Damsté, J. S., and Schouten, S.: Long chain 1,13- and 1,15-diols as a potential proxy for palaeotemperature reconstruction, 84, 204–216, https://doi.org/10.1016/j.gca.2012.01.024, 2012.

Rampen, S. W., Willmott, V., Kim, J.-H., Rodrigo–Gámiz, M., Uliana, R. E., Mollenhauer, G., Schefuß, E., Sinninghe

705 Damsté, J. S., and Schouten, S.: Evaluation of long chain 1,14-alkyl diols in marine sediments as indicators for upwelling and temperature., 76, 39–47, https://doi.org/10.1016/j.orggeochem.2014.07.012, 2014a.

Rampen, S. W., Datema, M., Rodrigo–Gámiz, M., Schouten, S., Reichart, G.-J., and Sinninghe Damsté, J. S.: Sources and proxy potential of long chain alkyl diols in lacustrine environments, 144, 59–71, https://doi.org/10.1016/j.gca.2014.08.033, 2014b.

710 Redfield, A. C., Ketchum, B. H., and Richards, F. A.: The influence of organisms on the composition of sea-water, in: The Sea, edited by: Hill, M. N., Interscience, New York, 26–77, 1963.

Romero, O. E., Baumann, K.-H., Zonneveld, K. A. F., Donner, B., Hefter, J., Hamady, B., Pospelova, V., and Fischer, G.: Flux variability of phyto– and zooplankton communities in the Mauritanian coastal upwelling between 2003 and 2008, 17, 187–214, https://doi.org/10.5194/bg-17-187-2020, 2020.

715 Sinninghe Damsté, J. S., Rampen, S., Rijpstra, W. I. C., Abbas, B., Muyzer, G., and Schouten, S.: A diatomaceous origin for long-chain diols and mid-chain hydroxy methyl alkanoates widely occurring in Quaternary marine sediments: Indicators for high-nutrient conditions, 67, 1339–1348, https://doi.org/10.1016/S0016-7037(02)01225-5, 2003.

Sollich, M., Yoshinaga, M. Y., Häusler, S., Price, R. E., Hinrichs, K.-U., and Bühring, S. I.: Heat stress dictates microbial lipid composition along a thermal gradient in marine sediments, Front. Microbiol., 8, 1550,

720 https://doi.org/10.3389/fmicb.2017.01550, 2017.

Suutari, M. and Laakso, S.: Microbial fatty acids and thermal adaptation, Critical Reviews in Microbiology, 20, 285–328, https://doi.org/10.3109/10408419409113560, 1994.

Tierney, J. E., Sinninghe Damsté, J. S., Pancost, R. D., Sluijs, A., and Zachos, J. C.: Eocene temperature gradients, 10, 538–539, https://doi.org/10.1038/ngeo2997, 2017.

725 Versteegh, G. J. M., Bosch, H. J., and de Leeuw, J. W.: Potential palaeoenvironmental information of C_{24} to C_{30} mid-chain diols, keto-ols and mid-chain hydroxy fatty acids; a critical review, 27, 1–13, https://doi.org/10.1016/S0146-6380(97)00063-6, 1997.

Versteegh, G. J. M., Jansen, J. H. F., de Leeuw, J. W., and Schneider, R. R.: Mid-chain diols and keto-ols in SE Atlantic sediments. A new tool for tracing past sea surface water masses?, 64, 1879–1892, https://doi.org/10.1016/S0016-

730 7037(99)00398-1, 2000.

Volkman, J. K., Barrett, S. M., Dunstan, G. A., and Jeffrey, S. W.: C_{30}–C_{32} alkyl diols and unsaturated alcohols in microalgae of the class Eustigmatophyceae, 18, 131–138, https://doi.org/10.1016/0146-6380(92)90150-V, 1992.

Volkman, J. K., Barrett, S. M., and Blackburn, S. I.: Eustigmatophyte microalgae are potential sources of C_{29} sterols, C_{22}–C_{28} n-alcohols and C_{28}- C_{32} n-alkyl diols in freshwater environments, 30, 307–318, https://doi.org/10.1016/S0146-

735 6380(99)00009-1, 1999.

Willmott, V., Rampen, S. W., Domack, E., Canals, M., Sinninghe Damsté, J. S., and Schouten, S.: Holocene changes in *Proboscia* diatom productivity in shelf waters of the north-western Antarctic Peninsula, 22, 3–10, https://doi.org/10.1017/S095410200999037X, 2010.

Zweng, M. M., Reagan, J. R., Seidov, D., Boyer, T. P., Locarnini, M. M., Garcia, H. E., Mishonov, A. V., and Baranova, O.
740   K.: World ocean atlas 2018, Vol. 2: Salinity, 2019.

Table 1. Deployment data of sediment trap CBeu

Mooring	Coordinates	GeoB No. cruise	Trap depth (m)	Ocean Bottom depth (m)	Sample amount	Capture duration (sample no. = days)	Sampling interval
1	20°45'N 18°42'W	- POS 310	1296	2714	20	1=10, 2–20=15.5	5 Jun 2003– 5 Apr 2004
2	20°45'N 18°42'W	9630-2 M 65-2	1296	2714	20	1–20=22 2–19=23	18 Apr 2004 – 20 Jul 2005
3	20°45.5'N 18°41.9'W	11404-3 POS 344-1	1277	2693	20	21.5	25 Jul 2005 – 28 Sept 2006
4	20°45.7'N 18°42.4'W	11835-2 MSM 04b	1256	2705	20	1=3.5 2–20=7.5	28 Oct 2006 – 23 Mar 2007
5	20°44.9'N 18°42.7'W	12910-2 POS 365-2	1263	2709	38	1,2=6.5 3–38=9.5	28 Mar 2007 – 17 Mar 2008

745

Table 2. Composition and position of the diols in the indices.

Index \ Diol	$1,13C_{28}$	$1,13C_{30}$	$1,15C_{30}$	$1,14C_{28}$	$1,14C_{30}$	$1,14C_{28:1}$[1]	$1,14C_{30:1}$
LDI	D	D	N				
DSI				N	N	D	D
DCI				D	N		
DI_R			D	N	N		
DI_W	D	D		N	N		
CDI	D	D	D	N	N		

Table 2. Composition and position of the diols in the indices.

Index \ Diol	$1,13C_{28}$	$1,13C_{30}$	$1,15C_{30}$	$1,14C_{28}$	$1,14C_{30}$	$1,14C_{28:1}$[1]	$1,14C_{30:1}$
NDI	D	D	D	N	D	N	D

Since all proxies are indices, all diols in the numerator (N) are also in the denominator (D).
[1]The $1,14C_{28:1}$ diol has not been detected in the CBeu1–5 samples

750

Table 3: Correlations of diol concentrations and their natural logarithms for CBeu1–5.

	Lipid	$1,13C_{28}$	$1,14C_{28}$	$1,13C_{30}$	$1,14C_{30:1}$	$1,14C_{30}$	$1,15C_{30}$	$1,15C_{32}$
			linear correlations[1] (r^2)					
	$1,13C_{28}$	—	*0.35*	*0.59*	*0.01*	*0.31*	*0.44*	*0.58*
	$1,14C_{28}$	0.42	—	*0.14*	*0.01*	*0.69*	*0.11*	*0.20*
	$1,13C_{30}$	0.75	0.29	—	*0.01*	*0.19*	*0.70*	*0.81*
natural	$1,14C_{30:1}$	0.18	0.17	0.14	—	*0.20*	*0.00*	*0.01*
logarithm	$1,14C_{30}$	0.58	0.83	0.50	0.33	—	*0.12*	*0.20*
correlati-	$1,15C_{30}$	0.62	0.36	0.82	0.14	0.51	—	*0.84*
ons[1] (r^2)	$1,15C_{32}$	0.70	0.34	0.84	0.17	0.51	0.85	—
	1,13 vs 1,14	0.48						
	1,13 vs 1,15	0.79						
	1,14 vs 1,15	0.45						

Outliers: $1,13C_{28}$ and $1,13C_{30}$ of CBeu1-4, CBeu3-18, CBeu4-18 and CBeu4-19 excluded. Colour coding: pink: 1,13 diols only, blue: 1,13+1,15 diols, green: 1,14 diols involved. Light colors correlations 0.5-0.74, dark colors correlations >0.74.
[1]Linear correlations in italics, natural logarithm based correlations in normal typeface.

755

Table 4: Correlations (r^2) between diol proxies and environment

	DI_W	DI_R	CDI	NDI	DCI	DSI	LDI
DI_R	**0.65**						
CDI	**0.69**	**1.00**					
NDI	**0.49**	**0.46**	**0.48**				
DCI	*0.32*	*0.15*	*0.16*	*0.74*			
DSI	0.080	*0.0004*	0.0005	**0.67**	*0.46*		
LDI	*0.036*	*0.27*	*0.24*	*0.029*	*0.0003*	0.09	
ln *P. alata* Flux	**0.12**	**0.29**	**0.29**	0.000	0.051	*0.019*	
Total Flux	0.011	0.024	0.021	0.001	*0.017*	*0.013*	
% Upw spp.	*0.20*	*0.07*	**0.09**	*0.38*	**0.42**	*0.39*	*0.02*
Wind Speed	*0.19 φ 79*	*0.11 φ 79*	*0.093 φ 35*	**0.28 φ 32**	**0.29 φ 30**	**0.24 φ 21**	
SST (lead)	*0.23 φ -69*	*0.10 φ -69*	*0.13 φ -69*	*0.38 φ -77*	0.29 φ -77	*0.42 φ -124*	(0.21 φ 140?)
SST (lag)	**0.27 φ 94**	0.13 φ 105	0.15 φ 104	0.34 φ 102	*0.35 φ 117*	0.25 φ 76	0.17 φ 41

Correlations with $p<0.05$ in bold, negative relations in italics. LDI outliers not included

760

765
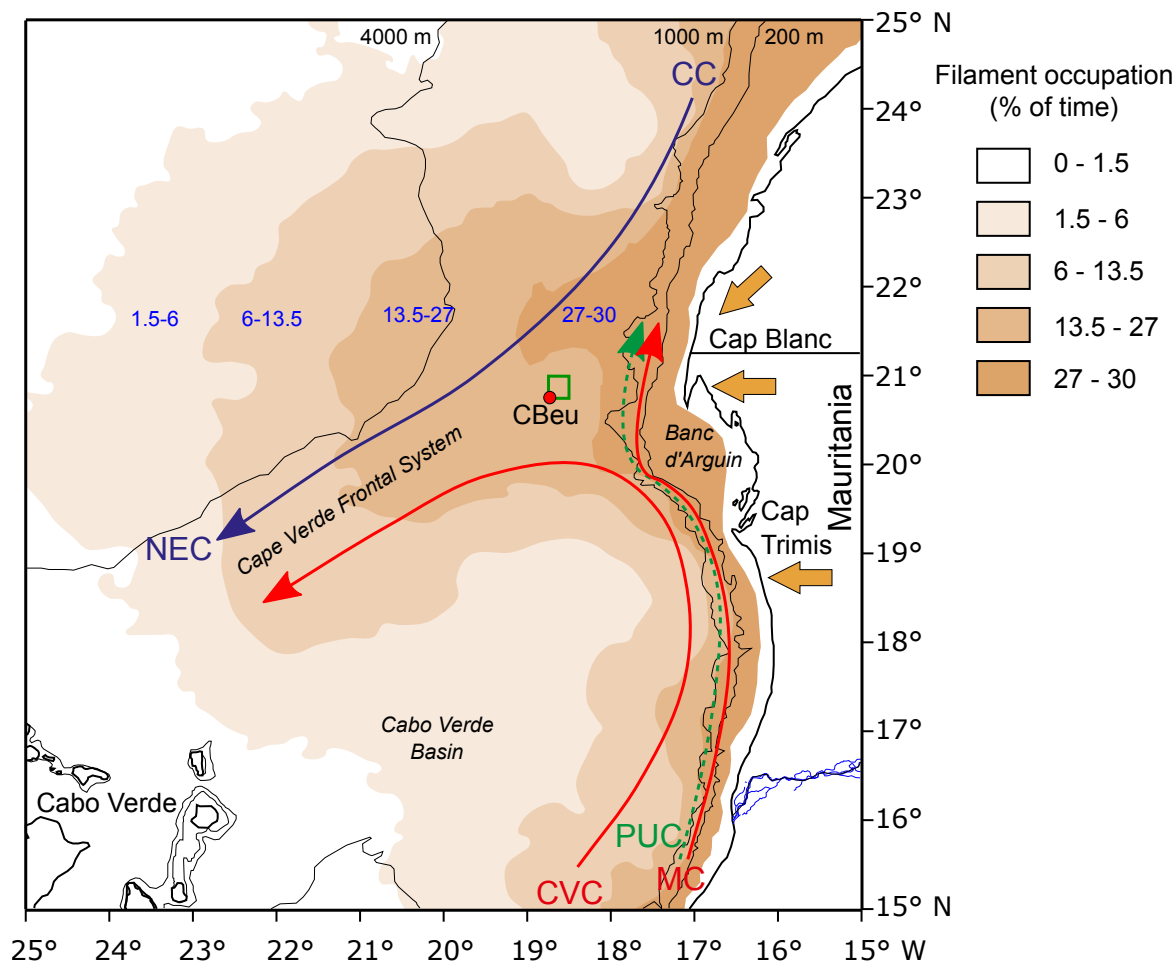
770   **Figure 1: The Mauritanian upwelling system. CC, Canary Current; NEC, North Equatorial Current; CVC, Cap Verde Current; MC, Mauritanian Current; PUC, Poleward Under Current. The red circle, in lower left corner of the small green square marks the location of mooring CBeu. The green square represents the upstream 0.25 x 0.25 degrees area from which sea surface data have been obtained.**

775
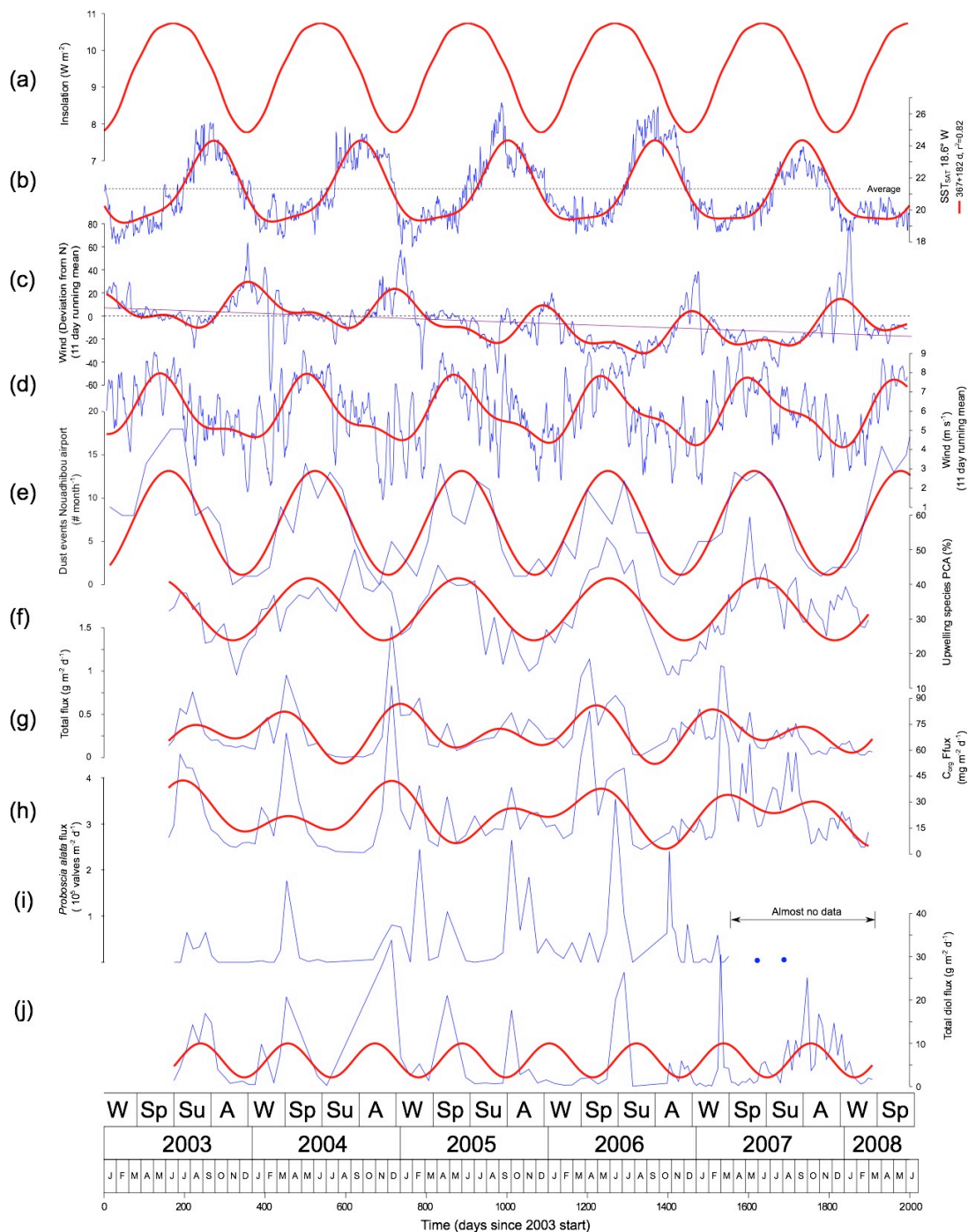
Figure 2: Variation of external variables and the total diol flux through time for CBeu1–5. Thin blue lines, measured values (for
780 **wind parameters 11 days running mean); Thick red lines, the most important frequency components. Note that most parameters**
have a dominant annual cycle modulated by a semiannual cycle. The Total Diol Flux (graph J) is dominated by a 257 days cycle.

785

790

795

800
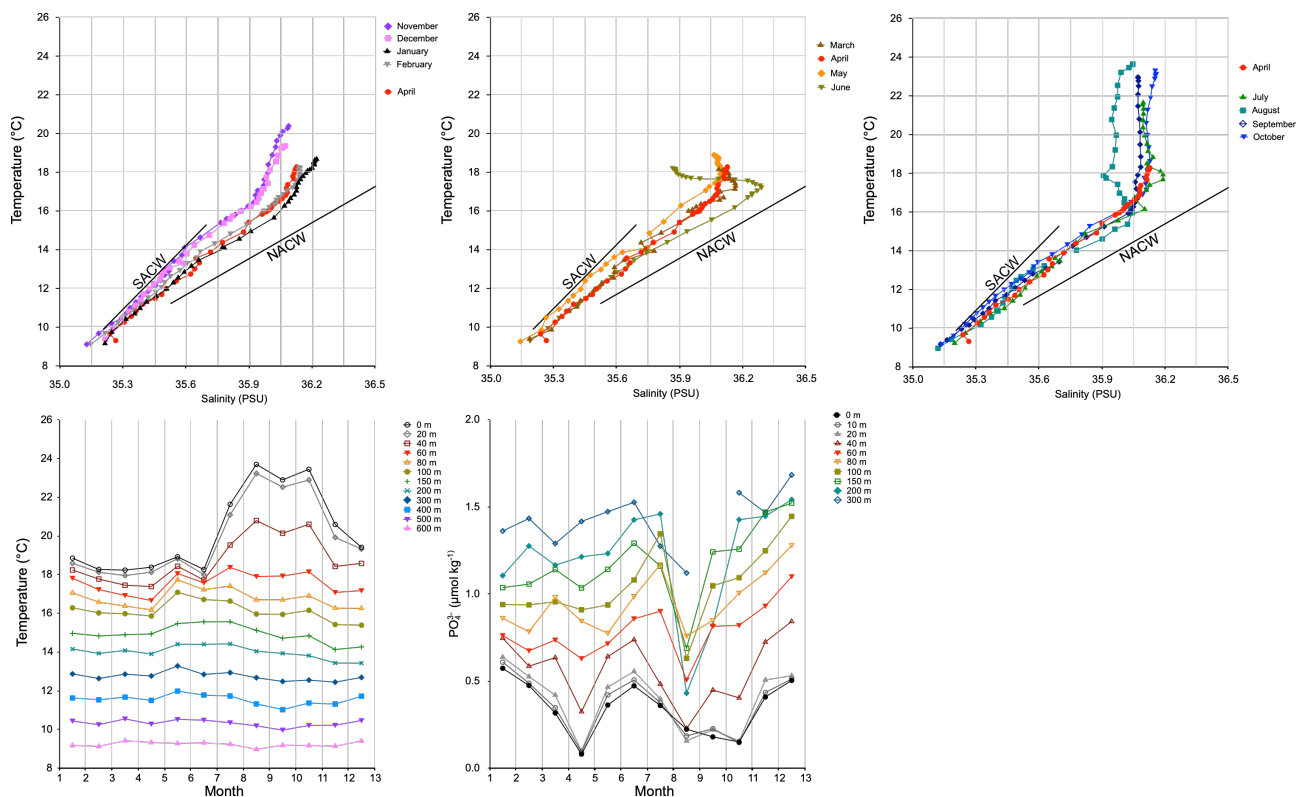
Figure 3: Oceanographic data from the World Ocean Atlas 2018 (WOA). Upper three panels, Temperature-Salinity diagrams for each month for the 1° square centered at 20.5°N, 18.5°W. Solid lines represent the North Atlantic Central Water (NACW) and the South Atlantic Central Water (SACW) (Locarini et al., 2018). Lower left panel, water temperatures for different depths in the same 1° square (Zweng et al., 2019). Lower right panel, monthly PO_4^{3-} concentrations against depth for the 5° square centered at 22.5°N, 17.5°W (Garcia et al., 2019).

805

810

815
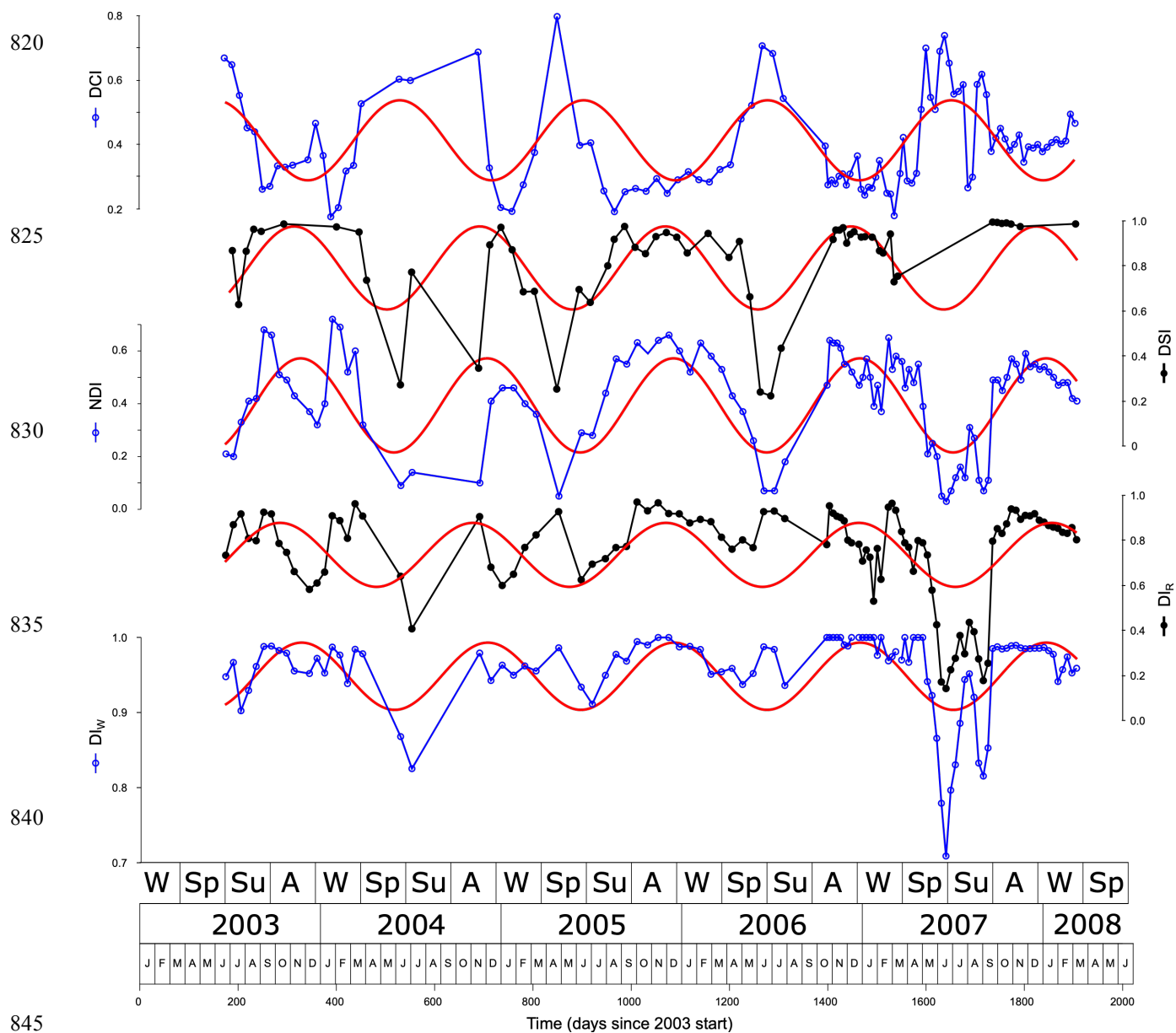
Figure 4: Diol proxies and their main (annual) frequency component. Note the close similarities between the diol proxies and the DCI behaving opposite to the others.
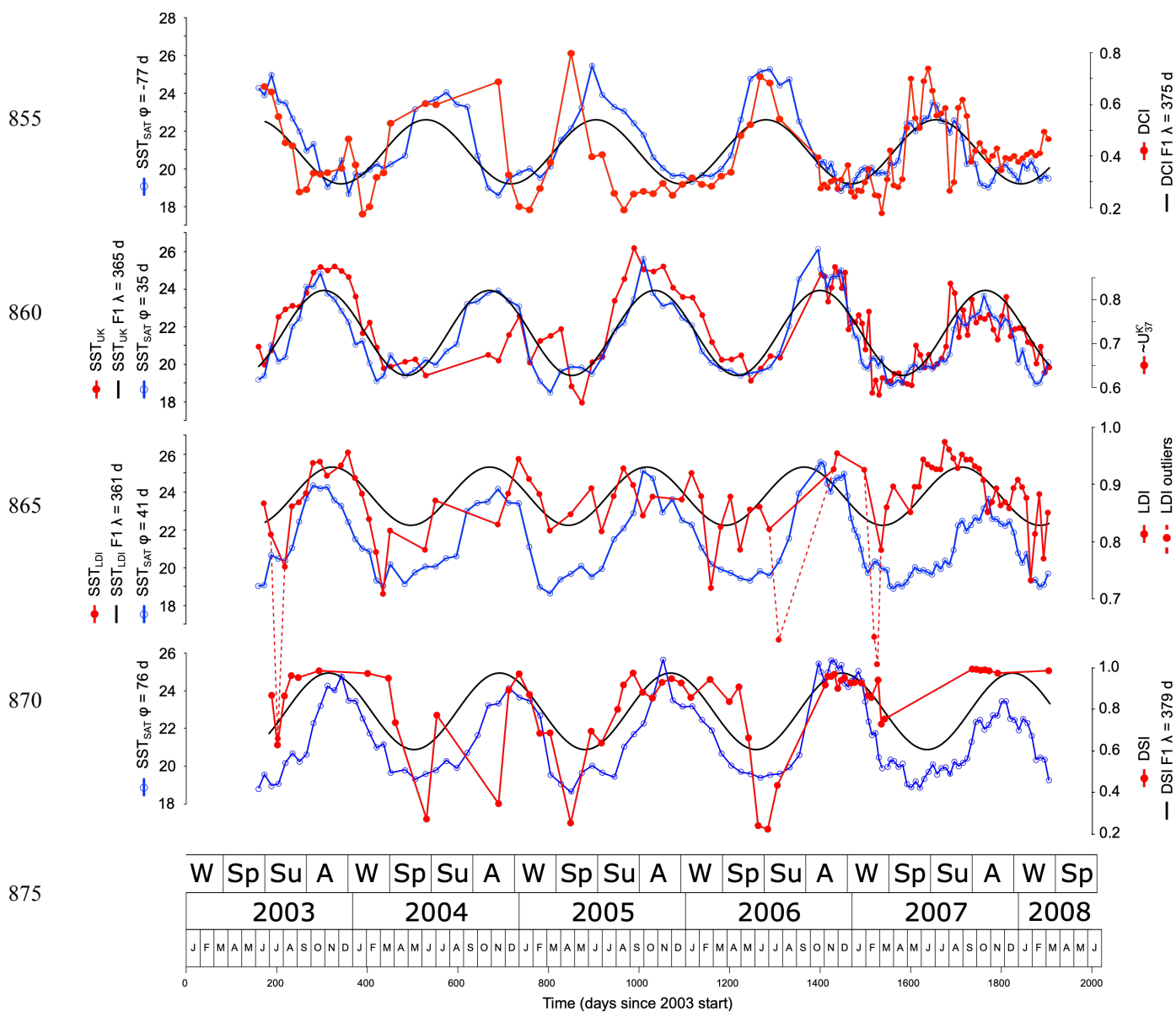
Figure 5: Proxy-derived SST (red, filled circles), their annual frequency component (F1,, black) and satellite-derived SST$_{SAT}$ (blue, empty circles). The phase shifts of the SST$_{SAT}$ are such that correlation with the proxy derived SST is highest. Corresponding proxy values are indicated on the right side of the panels. NB: check phase and λ LDI.

885
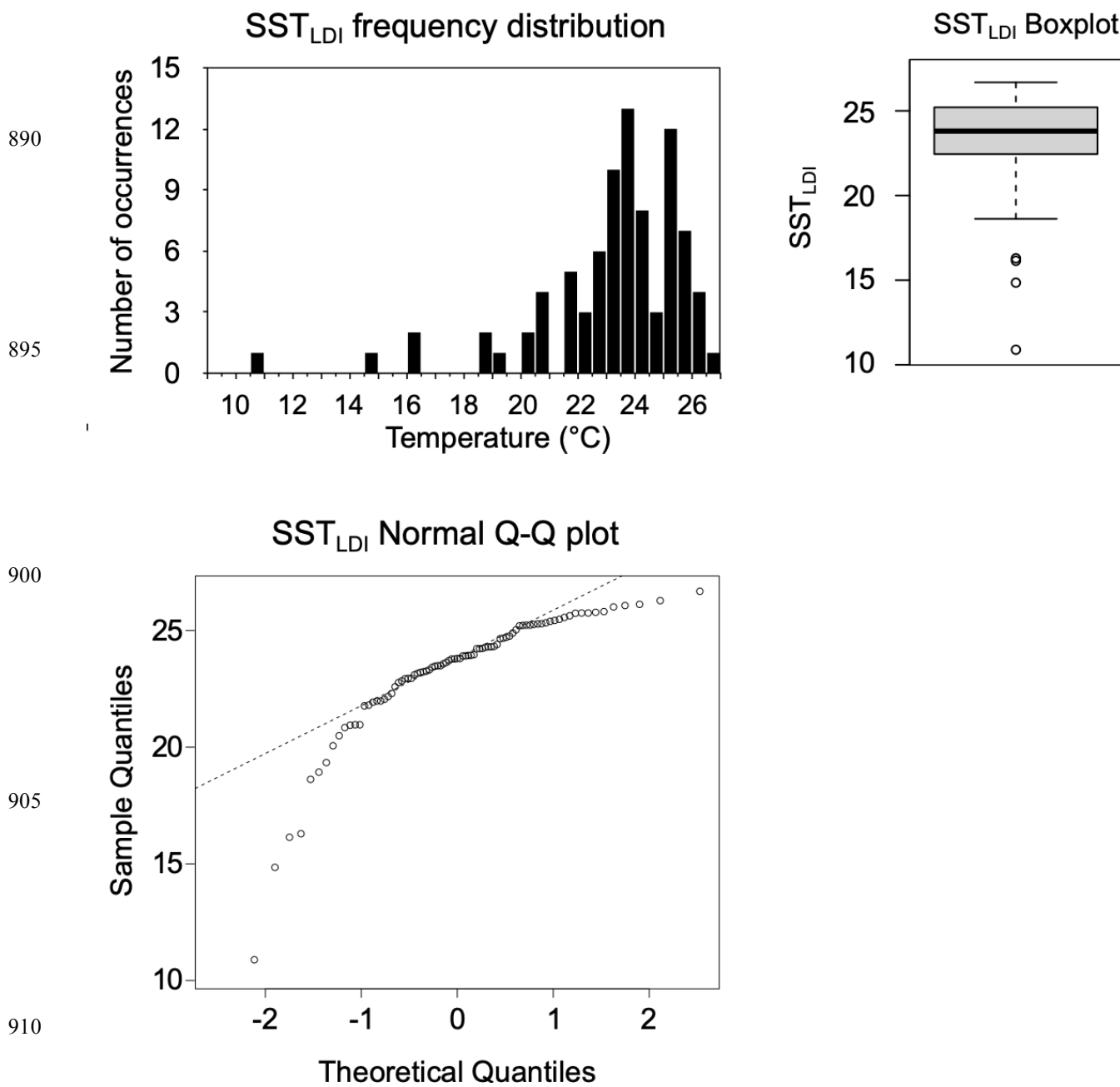
890

895

900

905

910

Figure 6: Statistics of the SST$_{LDI}$ values identifying the 5 values below 16°C as outliers. A. Frequency distribution; B. Boxplot; C. Q–Q plot, with dotted line representing the expected values for a normally distributed dataset.

915
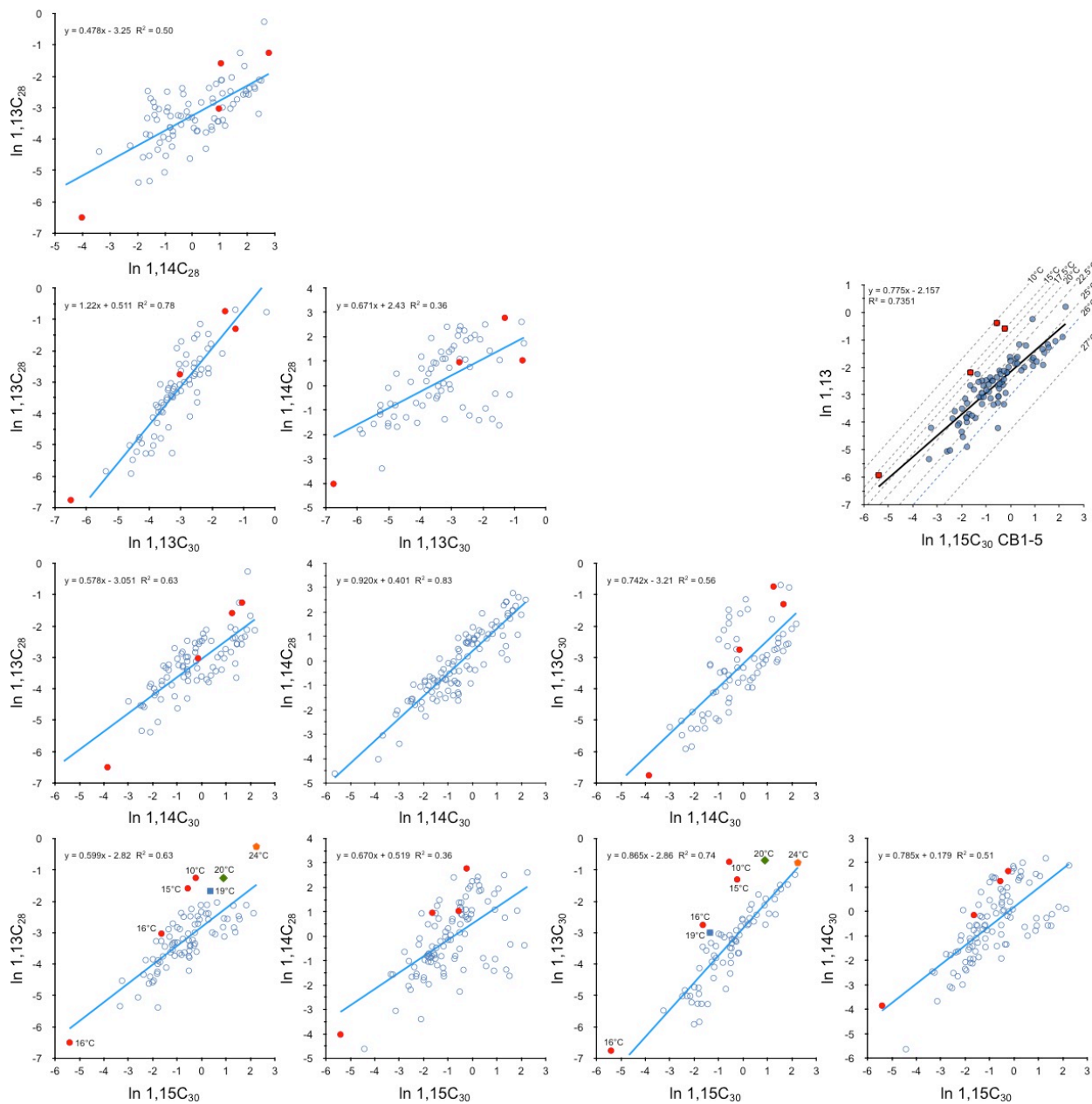
Figure 7: Cross plots of log transformed diol fluxes (µg m⁻² d⁻¹) with 1,13 diol values for samples providing SST_LDI values below 18°C in solid red red. These values have not been included for obtaining the (blue) regression lines. In the 1,13 x 1,15 diol plots other extreme points are indicated by a blue square (19°C), green diamond (20°C) and orange pentagram (24°C). Upper right plot, the diols involved in the LDI (1,15C_30 and combined 1,13 diols) are provided. The dotted lines represent isotherms for the transfer function of Rampen et al. (2012). The regression line shows how the (log transformed) composition of the diols involved in the LDI relates to temperature (excluding the outliers indicated in red).

920

925
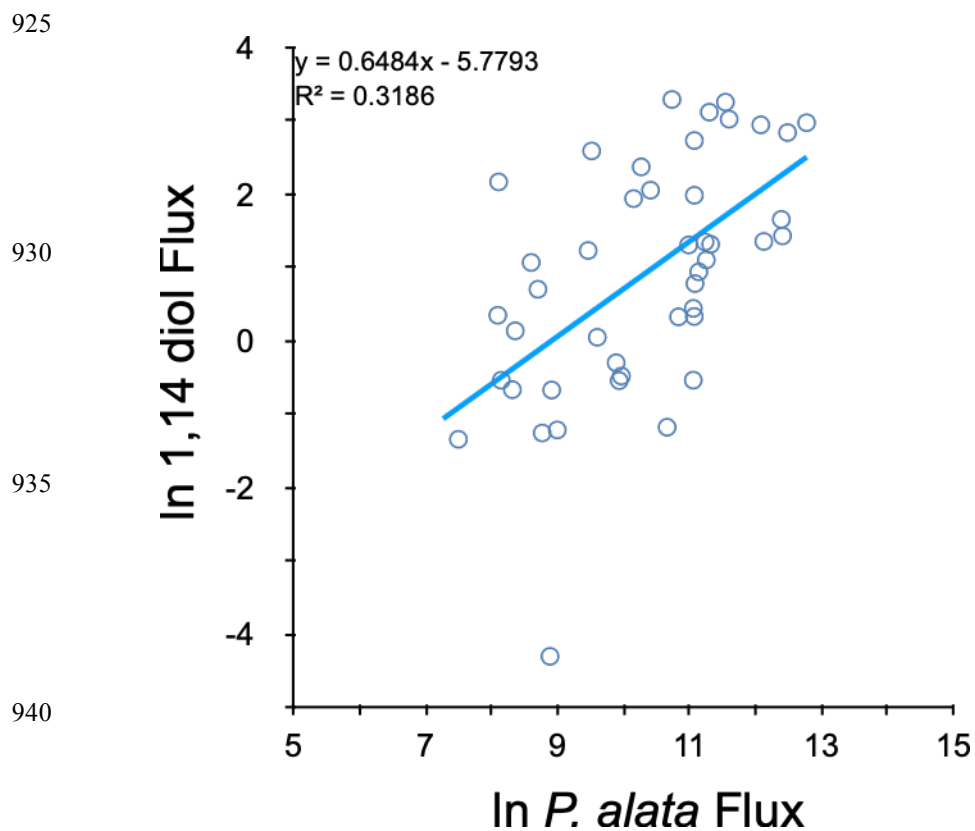
Figure 8: Correlation of natural logarithms of 1,14 diols fluxes (µg m⁻² d⁻¹) and diatom *Proboscia alata* fluxes (valves m⁻² d⁻¹).

945

950

955

Figure 9: Fluxes for individual diols in µg m⁻² d⁻¹.